

# Astroglial Kir4.1 in the lateral habenula drives neuronal bursts in depression

Yihui Cui<sup>1,2</sup>, Yan Yang<sup>1,2</sup>, Zheyi Ni<sup>1</sup>, Yiyan Dong<sup>1</sup>, Guohong Cai<sup>3</sup>, Alexandre Foncelle<sup>4,5</sup>, Shuangshuang Ma<sup>1</sup>, Kangning Sang<sup>1</sup>, Siyang Tang<sup>1</sup>, Yuezhou Li<sup>1</sup>, Ying Shen<sup>1</sup>, Hugues Berry<sup>4,5</sup>, Shengxi Wu<sup>3</sup> & Hailan Hu<sup>1,2</sup>

**Enhanced bursting activity of neurons in the lateral habenula (LHb) is essential in driving depression-like behaviours, but the cause of this increase has been unknown. Here, using a high-throughput quantitative proteomic screen, we show that an astroglial potassium channel (Kir4.1) is upregulated in the LHb in rat models of depression. Kir4.1 in the LHb shows a distinct pattern of expression on astrocytic membrane processes that wrap tightly around the neuronal soma. Electrophysiology and modelling data show that the level of Kir4.1 on astrocytes tightly regulates the degree of membrane hyperpolarization and the amount of bursting activity of LHb neurons. Astrocyte-specific gain and loss of Kir4.1 in the LHb bidirectionally regulates neuronal bursting and depression-like symptoms. Together, these results show that a glia–neuron interaction at the perisomatic space of LHb is involved in setting the neuronal firing mode in models of a major psychiatric disease. Kir4.1 in the LHb might have potential as a target for treating clinical depression.**

A major breakthrough in neuroscience was the discovery that astrocytes interact intimately with neurons to support and regulate essential functions and thereby foster information processing in the brain<sup>1–8</sup>. Many investigations have focused on astroglia–neuron interactions at tripartite synapses, where astrocyte processes wrap tightly around presynaptic and postsynaptic sites<sup>9</sup>. By contrast, less attention has been placed on astroglia–neuron interactions in proximity to the neuronal soma. In particular, how astrocytes regulate the intrinsic firing patterns of neurons, and what structural basis may underlie this regulation, have been much less explored.

Despite the surging interest in the role of the LHb in depression<sup>10–18</sup>, only limited attention has been given to the influence of astrocyte malfunction in the LHb on the aetiology of depression<sup>19</sup>. In an accompanying paper, we show that the bursting activity of LHb neurons is greatly enhanced in animal models of depression<sup>20</sup>. LHb bursting drives depressive-like behaviours and is a prominent target of the rapid antidepressant ketamine<sup>20</sup>. However, the cause of this enhanced bursting by LHb neurons remains unknown.

## LHb Kir4.1 is upregulated in depression

We used an unbiased, high-throughput, quantitative proteomic screen to compare habenular protein expression between congenitally learned helpless (cLH)<sup>21</sup> and wild-type Sprague–Dawley rats. Kir4.1 was highly upregulated in the habenulae of cLH rats<sup>14</sup> (1.69-fold of wild-type, Extended Data Fig. 1a). Western blot analysis confirmed that Kir4.1 was significantly increased (1.44-fold,  $P = 0.009$ ) in the membrane protein fraction of habenulae from cLH rats (Fig. 1a). By contrast, another astrocyte-specific protein, glial fibrillary acidic protein (GFAP), showed no change in expression (Extended Data Fig. 1b), indicating that there was no astrogliosis.

To test whether Kir4.1 upregulation is universal in depression, we examined rats in which depression was induced by treatment with lipopolysaccharide (LPS)<sup>22</sup>. One week of LPS injection (0.5 mg kg<sup>-1</sup> per day, intraperitoneal (i.p.)) was sufficient to cause strong depressive-like phenotype in three-month-old Wistar rats in the forced swim test (FST; Extended Data Fig. 1c)<sup>22</sup> and sucrose preference test (SPT)<sup>22</sup>.

Rats with LPS-induced depression also showed a significant increase in Kir4.1 in the habenula (1.87-fold,  $P < 0.0001$ , Fig. 1b). Quantitative real-time PCR revealed an increase (1.2-fold) in *Kir4.1* (also known as *Kcnj10*) mRNA level in habenulae from cLH rats (Extended Data Fig. 1d), suggesting that at least part of the change in protein level is due to transcriptional upregulation.

Kir4.1 is a principal component of the glial Kir channel and is largely responsible for mediating the K<sup>+</sup> conductance and setting the

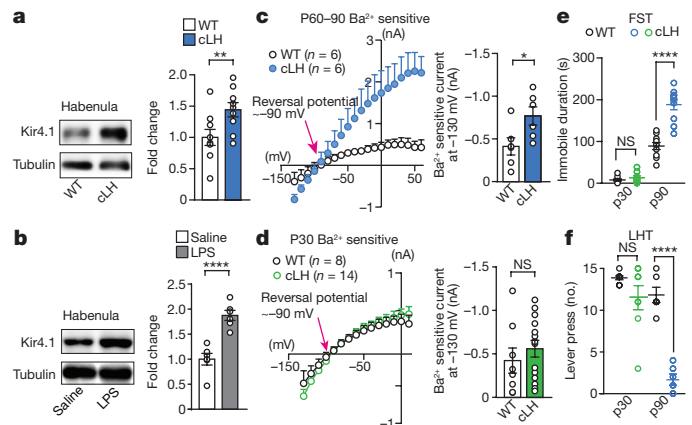


**Figure 1 | Kir4.1 is upregulated in the LHb in rat models of depression.**

**a, b**, Western blot analysis showing upregulation of Kir4.1 protein in membrane fraction of habenulae of cLH rats ( $n = 9$ , 9 rats for WT and cLH, respectively, **a**) and rats with LPS-induced depression ( $n = 6$ , 6, **b**). Tubulin is used as loading control. WT, wild-type Sprague–Dawley rats. **c, d**,  $I$ – $V$  plot and bar graph showing Ba<sup>2+</sup>-sensitive currents in cLH rats and wild-type controls at the age of P60–90 (**c**) and P30 (**d**). **e, f**, Age-dependent FST (**e**) and LHT (**f**) phenotypes of cLH rats.  $n = 8$ , 8 rats for P30,  $n = 10$ , 10; 6, 6 rats for P90 FST and LHT, respectively. Data are means  $\pm$  s.e.m. \* $P < 0.05$ , \*\* $P < 0.01$ , \*\*\*\* $P < 0.0001$ ; NS, not significant. Two-tailed paired  $t$ -test (**a, b**), two-tailed unpaired  $t$ -test (**c, e, f**) and Mann–Whitney test (**d**).

<sup>1</sup>Center for Neuroscience, Key Laboratory of Medical Neurobiology of the Ministry of Health of China, School of Medicine, Interdisciplinary Institute of Neuroscience and Technology, Qishui Academy for Advanced Studies, Zhejiang University, Hangzhou 310058, China. <sup>2</sup>Mental Health Center, School of Medicine, Zhejiang University, Hangzhou 310013, China. <sup>3</sup>Department of Neurobiology, School of Basic Medicine, Fourth Military Medical University, Xi'an 710032, China. <sup>4</sup>INRIA, Lyon, F-69603, France. <sup>5</sup>University of Lyon, UMR 5205, CNRS, LIRIS, F-69622, France.

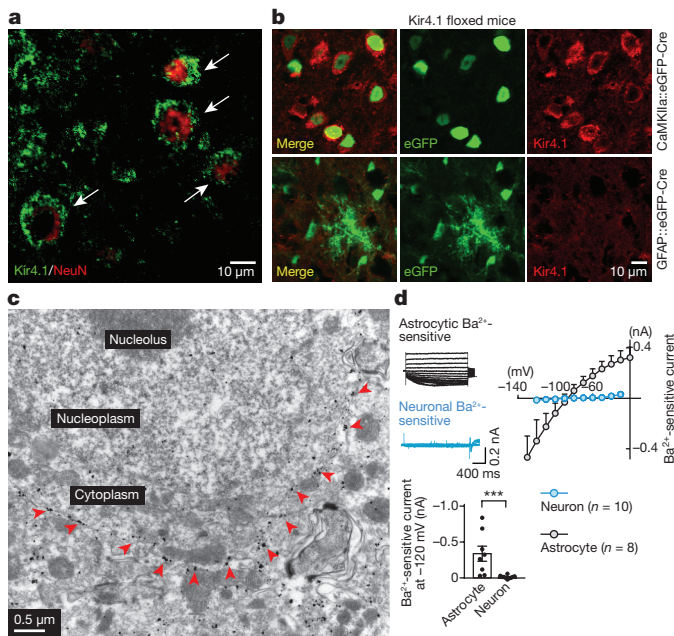


**Figure 2 | Kir4.1 is expressed on astrocytic processes that wrap tightly around neuronal somata in LHB.** **a**, Immunohistochemistry signals of Kir4.1 envelope neuronal somata as indicated by white arrows (three independent experiments). **b**, The pan-soma Kir4.1 signals remain intact in the LHB of Kir4.1 floxed mice injected with AAV-CaMKIIa::eGFP-Cre, but are eliminated in mice injected with AAV-GFAP::eGFP-Cre (three independent experiments). **c**, Immunogold electron microscopy of Kir4.1. Red arrows indicate gold signals surrounding a neuronal soma (three independent experiments). **d**, I–V plots of the Ba<sup>2+</sup>-sensitive Kir4.1 current recorded in LHB astrocytes and neurons. Top left, representative traces; bottom left, bar graph of current recorded when cells are held at –120 mV. Two-tailed Mann–Whitney test. Data are means ± s.e.m. \*\*\**P* < 0.001.

resting membrane potential (RMP) in astrocytes<sup>23–25</sup>. To confirm that Kir4.1 function is indeed upregulated in rat models of depression, we performed whole-cell patch-clamp recordings onto LHB astrocytes from cLH or wild-type rats. Astrocytes were distinguished from neurons by their small (5–10 μm), oval somata and electrophysiological features (Extended Data Fig. 2a–d; see Methods). Biocytin filling and the absence of NeuN co-staining confirmed that cells fitting the above criteria were indeed astrocytes (Extended Data Fig. 3). We then bath-applied Ba<sup>2+</sup> (BaCl<sub>2</sub>, 100 μM), which selectively blocks Kir channels at sub-millimolar concentrations, to isolate Kir4.1 current<sup>24</sup> (Extended Data Fig. 2a, c). The Ba<sup>2+</sup>-sensitive current displayed a reversal potential close to the equilibrium potential of K<sup>+</sup> (*E*<sub>K</sub>) (–90 mV)<sup>23,24</sup> (Fig. 1c, d), indicating that it represents the K<sup>+</sup> conductance. We found that Ba<sup>2+</sup>-sensitive currents in LHB astrocytes were almost doubled in astrocytes from cLH (Fig. 1c) and LPS-treated rats (Extended Data Fig. 2f) at postnatal days (P)60–90.

Notably, the increase in Kir4.1 current and protein level was not obvious in cLH rats at P30 (Fig. 1d, Extended Data Fig. 1e). At this age, cLH rats did not yet show depression-like phenotypes in either the FST (Fig. 1e) or the learned helplessness test (LHT; Fig. 1f), suggesting that the upregulation of Kir4.1 is concomitant with the developmental onset of the depression-like symptoms.

### Kir4.1 on astrocytes encircles neuronal soma

As an inwardly rectifying K<sup>+</sup> channel, Kir4.1 has been strongly implicated in buffering excess extracellular K<sup>+</sup> in tripartite synapses<sup>25–28</sup>. The conventional model of K<sup>+</sup> buffering suggests that Kir4.1 is highly expressed in astrocytic endfeet surrounding synapses<sup>29,30</sup>. Unexpectedly, immunohistochemical staining for Kir4.1 in the LHB appeared to overlap with the neuronal marker NeuN at low

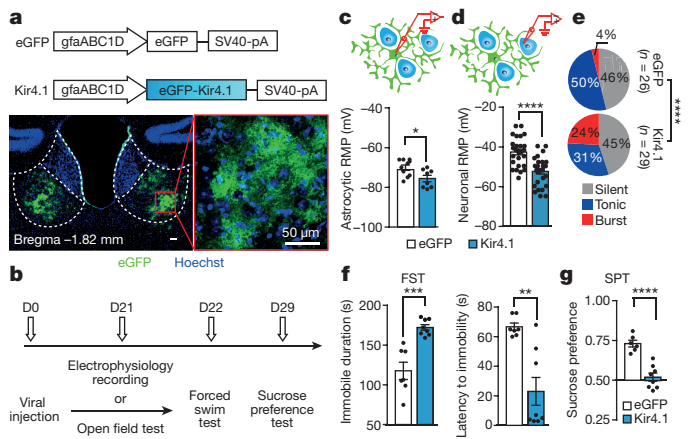


**Figure 3 | Astrocytic kir4.1 overexpression increases neuronal bursts in the LHB and causes depression-like phenotypes.** **a**, Top, schematics of AAV vectors engineered to overexpress Kir4.1 or eGFP control under a *GFAP* promoter. Bottom, illustration of bilateral viral injection of AAV-GFAP::Kir4.1 in mouse LHB (stained with antibody against GFP and Hoechst) (four independent experiments). **b**, Experimental paradigm for electrophysiology and behavioural testing. **c–e**, Astrocytic overexpression of Kir4.1 decreases RMPs of both astrocytes (*n* = 10, 8 astrocytes from 4, 3 mice for eGFP and Kir4.1, respectively, **c**) and neurons (*n* = 26, 29 neurons from 6, 6 mice, **d**) and increases the bursting population in neurons (**e**). **f, g**, Behavioural effects of expression of various viral constructs in the LHB in the FST (*n* = 7, 8 mice, **f**) and SPT (*n* = 6, 8 mice, **g**). Data are means ± s.e.m. \**P* < 0.05, \*\**P* < 0.01, \*\*\**P* < 0.001, \*\*\*\**P* < 0.0001. Two-tailed unpaired *t*-test (**c, d, f, g**) and  $\chi^2$  test (**e**).

magnification (20×; Extended Data Fig. 4a), although in the same brain slice Kir4.1 staining in the hippocampus showed a typical astrocytic appearance (Extended Data Fig. 4b). However, higher magnification imaging with single-layer scanning (0.76 μm per layer) revealed that Kir4.1 staining enveloped NeuN signals (Fig. 2a). To confirm that Kir4.1 was located within astrocytes but not neurons in the LHB, we separately knocked it out in either neurons or astrocytes by injecting AAV viruses expressing the Cre recombinase under either the neuronal *Camk2a* promoter or the glial *GFAP* promoter (*gfaABC1D*)<sup>7,31</sup> into Kir4.1 floxed (*Kcnj10*<sup>fl/fl</sup>) mice<sup>24</sup>. Neuronal knockout of Kir4.1 expression did not change the pattern of Kir4.1 staining, but astrocytic knockout completely eliminated it (Fig. 2b). Electron microscopy imaging revealed that Kir4.1-positive gold particles encircled the membrane of neuronal cell bodies (Fig. 2c, Extended Data Fig. 5a, b) as well as synapses (Extended Data Fig. 5c). Consistently, whole-cell patch-clamp recordings showed that Ba<sup>2+</sup>-sensitive currents were absent from neurons but abundant in astrocytes in the LHB (Fig. 2d, Extended Data Fig. 6). Together these results suggest that Kir4.1 is mainly expressed in astrocytic processes that wrap tightly around neuronal somata and synapses in the LHB.

### Kir4.1 gain-of-function causes depression

To test the consequences of Kir4.1 upregulation in the LHB, we used adeno-associated viruses of the 2/5 serotype (AAV2/5), which preferentially target astrocytes<sup>7</sup>, together with the human *GFAP* (*gfaABC1D*) promoter<sup>7,31</sup> to deliver eGFP-tagged Kir4.1 channel (AAV-GFAP::Kir4.1) or eGFP alone (AAV-GFAP::eGFP) as a control (Fig. 3a). Twenty-one days after bilateral injection into the LHB at P50, AAV2/5-mediated viral transfection led to expression of Kir4.1 and eGFP in astrocytes throughout the LHB (Fig. 3a). The specificity of the viral infection in astrocytes was verified by co-immunostaining of NeuN and eGFP: only 0.3% of NeuN<sup>+</sup> cells (*n* = 2,668) were infected by this virus (Extended Data Fig. 7a). We made whole-cell patch-clamp recordings from either astrocytes or neurons surrounding the virally transfected astrocytes in coronal LHB slices (Fig. 3b–e). The RMPs of

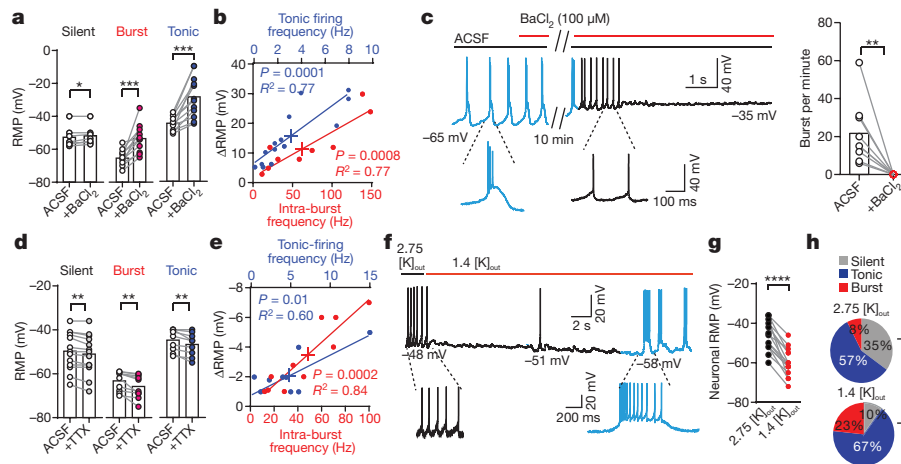


**Figure 4 | Kir4.1-dependent potassium buffering regulates neuronal RMP and bursting in LHB.** **a, d,** Changes in neuronal RMPs caused by BaCl<sub>2</sub> (100 μM, *n* = 7, 11, 12 neurons from 3, 3, 3 rats for silent, bursting and tonic, respectively, **a**) or TTX (1 μM, *n* = 13, 9, 9 neurons from 2, 2, 2 rats, **d**) in different neuronal types. RMPs were measured 15 min or 5 min after perfusion with BaCl<sub>2</sub> or TTX, respectively, when the RMPs had stabilized. **b, e,** Changes in neuronal RMPs after BaCl<sub>2</sub> (*n* = 14, 9 neurons from 3, 3 rats for tonic and burst group, respectively, **b**) or TTX (*n* = 9, 9 neurons from 2, 2 rats, **e**) treatment correlate with original firing rates of tonic-firing neurons (blue) or intra-burst frequencies of bursting neurons (red). **c,** Representative trace (left) and bar graph (right, 9 neurons from

3 rats) showing effect of BaCl<sub>2</sub> (15 min after drug perfusion) on bursting neurons. Spikes in bursting and tonic firing modes are shown in blue and black, respectively. **f,** Example of LHB neurons transforming from tonic-firing to burst-firing mode after [K]<sub>out</sub> is reduced from normal (2.75 mM) by 50% (to 1.4 mM). **g, h,** Reducing [K]<sub>out</sub> by 50% decreases neuronal RMPs (*n* = 15 neurons from 4 rats, sampled 1 min after change in [K]<sub>out</sub>, **g**) and increases bursting neural population (*n* = 33, 40 neurons from 4, 6 rats for normal and reduced [K]<sub>out</sub>, respectively, **h**). Data are means ± s.e.m. \**P* < 0.05, \*\**P* < 0.01, \*\*\**P* < 0.001, \*\*\*\**P* < 0.0001. Two-tailed paired *t*-test (**a, c, d, g**), χ<sup>2</sup> test (**h**) and linear regression test (**b, e**).

both astrocytes and neurons were more hyperpolarized (Fig. 3c, d) and the percentage of bursting neurons was significantly higher (Fig. 3e, *P* < 0.0001) in mice infected with AAV-GFAP::Kir4.1 than in mice infected with AAV-GFAP::eGFP.

We then assayed depression-like phenotypes and found that mice with AAV-GFAP::Kir4.1 infection in the LHB displayed severe depression-like behaviours, including increased immobile duration and decreased latency to immobility in the FST (Fig. 3f), and decreased sucrose preference in the SPT (Fig. 3g), while general locomotion was unchanged (Extended Data Fig. 7c, d).

### Kir4.1 regulates neuronal RMP and bursting

How does an astrocytic K<sup>+</sup> channel regulate the RMP and burst firing of LHB neurons? We hypothesize that within the highly confined extracellular space between neuronal somata and Kir4.1-positive astrocytic processes (Fig. 2), the constantly released K<sup>+</sup> from intrinsically active LHB neurons is quickly cleared by astrocytes through a Kir4.1-dependent mechanism. Accordingly, we predict that blockade of Kir4.1 should compromise spatial buffering of K<sup>+</sup>, resulting in increased extracellular K<sup>+</sup> ([K]<sub>out</sub>), and according to the Nernst equation, depolarized neuronal RMPs (modelled in Extended Data Fig. 8). Consistent with this prediction, blockage of Kir4.1 by bath perfusion with BaCl<sub>2</sub> for about 10 min depolarized the RMPs of LHB neurons (Fig. 4a). The degree of change in RMP positively correlated with the original firing rates of neurons (Fig. 4b), indicating that the more active the neuron is, the larger contribution the K<sup>+</sup> buffering makes to its RMP. A similar amount of RMP change was induced when BaCl<sub>2</sub> was applied in the presence of synaptic transmission blockers (picrotoxin, 1,2,3,4-tetrahydro-6-nitro-2,3-dioxo-benzo[*f*]quinoxaline-7-sulfonamide (NBQX) and 2-amino-5-phosphonopentanoic acid (AP5); Extended Data Fig. 9a–c), suggesting that Kir4.1-dependent regulation of RMP in LHB neurons occurs mostly at neuronal cell bodies instead of at synapses. Consequent to the RMP change and accumulation of [K]<sub>out</sub>, perfusion with BaCl<sub>2</sub> caused either a shift in the spiking pattern from bursting to tonic firing and eventually to cessation of neuronal activity (5 of 9 neurons; Fig. 4c), or a prolonged plateau potential within a burst and eventually cessation of bursting firing (4 of 9 neurons; Extended Data Fig. 9d).

By contrast, upregulation of Kir4.1 or prevention of neuronal firing should decrease [K]<sub>out</sub> and hyperpolarize neuronal RMPs. Indeed, overexpression of Kir4.1 in astrocytes (Fig. 3d) or blockage of neuronal action potentials by tetrodotoxin (TTX; Fig. 4d, e) caused hyperpolarization of LHB neurons. Overexpression of Kir4.1 in astrocytes also increased neuronal bursting (Fig. 3e). Finally, to assess a causal relationship between [K]<sub>out</sub> and firing mode, we made current-clamp recordings from LHB neurons while lowering [K]<sub>out</sub> by 50% (from 2.75 mM to 1.4 mM, Fig. 4f). This led to a reduction in neuronal RMP of 13.7 ± 0.5 mV (Fig. 4g) and a direct shift of originally tonic-firing neurons (8 out of 15) into bursting mode. Consequently, the percentage of bursting neurons was increased from 8% to 23% (Fig. 4h). Thus, by increasing astrocytic Kir4.1 expression or decreasing extracellular K<sup>+</sup> concentration, we were able to phenocopy in wild-type animals several key neuronal properties observed in the LHB of animal models of depression, namely hyperpolarized RMPs and enhanced bursts. These results indicate that enhanced extracellular K<sup>+</sup> clearance resulting from overexpression of Kir4.1 might underlie the neuronal hyperpolarization required for burst initiation.

### Kir4.1 loss-of-function rescues depression

To determine whether loss-of-function of Kir4.1 in the LHB could reduce neuronal bursts and reverse depressive phenotypes, we devised two strategies. We used AAV2/5 viral vectors to express either a short hairpin RNA (shRNA) to knock down the level of Kir4.1, or a dominant-negative construct to block its function, in the LHB of cLH rats (Fig. 5a). We tested six shRNAs that specifically targeted the Kir4.1 transcript in cell culture and chose the one with highest knockdown efficiency (Fig. 5b and Extended Data Fig. 10a) for viral packaging. To avoid an off-target effect of the shRNA, we also used a dominant-negative form of Kir4.1 (dnKir4.1), which contains a GYG-to-AAA point mutation at the channel pore, which blocks K<sup>+</sup> channels<sup>32</sup> (Fig. 5a, c, Extended Data Figs 7b, 10b). We first examined the effect of Kir4.1-shRNA on glial and neural electrophysiological properties. In astrocytes infected with AAV-H1::Kir4.1-shRNA, we observed a marked change in the current–voltage (*I*–*V*) relationship (Fig. 5d) and a depolarization of 41 mV compared with astrocytes infected with control shRNA (Fig. 5e), consistent with previous findings that Kir4.1 is mainly responsible for

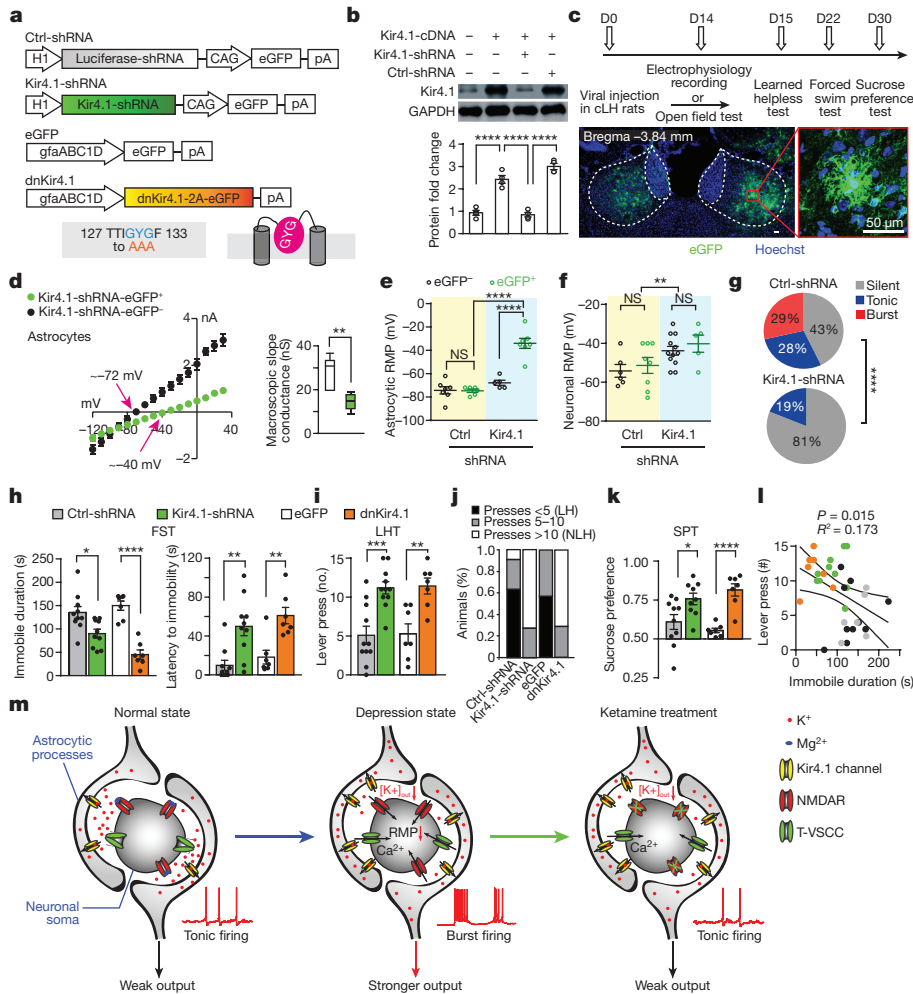


**Figure 5 | Loss of function of Kir4.1 in Lhb decreases neuronal bursting and rescues depression-like phenotypes of cLH rats.** **a**, Schematics of the AAV vector engineered to overexpress shRNA or dominant-negative Kir4.1. H1, human H1 promoter; CAG, CMV early enhancer/chicken *Actb* promoter. Three point mutations in the dnKir4.1 and their locations in the channel pore are shown below. **b**, Western blot and quantification showing efficient knockdown of Kir4.1 by shRNA in HEK293TN cells. **c**, Top, experimental paradigm for behavioural testing; bottom, illustration of bilateral expression of AAV-GFP::dnKir4.1 in Lhb (stained with antibodies against GFP and Hoechst). **d–g**, AAV-Kir4.1-shRNA caused a shift in reversal potential from  $-72$  to  $-40$  mV in astrocytes (**d**), depolarized astrocytes (**e**) and neurons in viral infected region (**f**), and abolished neuronal bursting (**g**). Floating bars for membrane slope conductance in **d** are calculated from the  $I-V$  plots (between  $-120$  and

$+40$  mV). **h–k**, Behavioural effects of expression of various viral constructs in the Lhb of cLH rats in the FST (**h**), LHT (**i**, **j**) and SPT (**k**). **j**, Percentage of rats in each category. LH, learned helpless rats with  $<5$  lever presses; NLH, non-learned helpless rats with  $>10$  lever presses. **l**, FST immobility is highly correlated with learned helplessness phenotype. **m**, A model for mechanisms of depression and ketamine treatment in the Lhb. Upregulation of Kir4.1 on astrocytic processes surrounding neuronal somata leads to enhanced  $K^+$  buffering at the tight neuron–glia junction, decreased  $[K]_{out}$  and hyperpolarized neuronal RMP. Consequently, de-inactivation of T-VSCCs initiates NMDAR-dependent bursts, causing a stronger output of Lhb to trigger depression. Ketamine blockade of NMDARs stops bursting and relieves depression. Data are means  $\pm$  s.e.m. \* $P < 0.05$ , \*\* $P < 0.01$ , \*\*\* $P < 0.001$ , \*\*\*\* $P < 0.0001$ , NS, not significant. (See Supplementary Table 1 for statistical analysis and  $n$  numbers.)

setting astrocytic RMPs<sup>24</sup>. The RMPs of neurons infected with AAV-H1::Kir4.1-shRNA did not differ from those of neighbouring non-infected neurons (because neurons do not express Kir4.1 endogenously, Fig. 5f). However, the RMPs of neighbouring Lhb neurons in AAV-H1::Kir4.1-shRNA-infected brain slices were overall more depolarized than the RMPs of neurons from rats infected with the control shRNA (Fig. 5f), suggesting that knock-down of Kir4.1 in astrocytes had a widespread impact on the RMPs of neighbouring neurons. Similar effects were observed in Lhb slices infected with AAV-GFAP::dnKir4.1 (Extended Data Fig. 10c–f). Notably, bursting activity in the Lhb of cLH rats was eliminated by infection with AAV-H1::Kir4.1-shRNA (Fig. 5g) or AAV-GFAP::dnKir4.1 (Extended Data Fig. 10f).

Behaviourally, infection with AAV-H1::Kir4.1-shRNA or AAV-GFAP::dnKir4.1 caused a pronounced reduction in the depression-like phenotypes of cLH rats in three depression paradigms: it reduced immobility in the FST (Fig. 5h), increased bar pressing number

in the LHT (Fig. 5i, j), and increased sucrose preference in the SPT (Fig. 5k). The behaviour scores in the LHT correlated with those in the FST (Fig. 5l).

**Concluding remarks**

Here we describe an important function of Kir4.1 in regulating neuronal RMP and firing pattern at the highly specialized neuron–glia interface in the Lhb. During depression, upregulation of Kir4.1 may cause enhanced extracellular  $K^+$  clearance, leading to a decrease in  $[K]_{out}$  and neuronal hyperpolarization (Fig. 5m). As demonstrated in the accompanying publication<sup>20</sup>, neuronal hyperpolarization may de-inactivate T-type voltage-sensitive calcium channels (T-VSCCs), which in turn initiate NMDAR-dependent bursts and thereby increase suppression of downstream monoaminergic centres (Fig. 5m). These results may inspire the development of new treatments for major depression targeting maladaptive neuron–glia interactions in the Lhb.

We also expect that the perisomatic K<sup>+</sup> buffering mechanism described here may have a more widespread function.

**Online Content** Methods, along with any additional Extended Data display items and Source Data, are available in the online version of the paper; references unique to these sections appear only in the online paper.

**Received 19 May 2017; accepted 12 January 2018.**

- Volterra, A. & Meldolesi, J. Astrocytes, from brain glue to communication elements: the revolution continues. *Nat. Rev. Neurosci.* **6**, 626–640 (2005).
- Attwell, D. *et al.* Glial and neuronal control of brain blood flow. *Nature* **468**, 232–243 (2010).
- Giaume, C., Koulakoff, A., Roux, L., Holcman, D. & Rouach, N. Astroglial networks: a step further in neuroglial and gliovascular interactions. *Nat. Rev. Neurosci.* **11**, 87–99 (2010).
- Halassa, M. M. & Haydon, P. G. Integrated brain circuits: astrocytic networks modulate neuronal activity and behavior. *Annu. Rev. Physiol.* **72**, 335–355 (2010).
- Molofsky, A. V. *et al.* Astrocytes and disease: a neurodevelopmental perspective. *Genes Dev.* **26**, 891–907 (2012).
- Woo, D. H. *et al.* TREK-1 and Best1 channels mediate fast and slow glutamate release in astrocytes upon GPCR activation. *Cell* **151**, 25–40 (2012).
- Tong, X. *et al.* Astrocyte Kir4.1 ion channel deficits contribute to neuronal dysfunction in Huntington's disease model mice. *Nat. Neurosci.* **17**, 694–703 (2014).
- Khakh, B. S. & Sofroniew, M. V. Diversity of astrocyte functions and phenotypes in neural circuits. *Nat. Neurosci.* **18**, 942–952 (2015).
- Araque, A., Parpura, V., Sanzgiri, R. P. & Haydon, P. G. Tripartite synapses: glia, the unacknowledged partner. *Trends Neurosci.* **22**, 208–215 (1999).
- Sartorius, A. *et al.* Remission of major depression under deep brain stimulation of the lateral habenula in a therapy-refractory patient. *Biol. Psychiatry* **67**, e9–e11 (2010).
- Li, B. *et al.* Synaptic potentiation onto habenula neurons in the learned helplessness model of depression. *Nature* **470**, 535–539 (2011).
- Lammel, S. *et al.* Input-specific control of reward and aversion in the ventral tegmental area. *Nature* **491**, 212–217, (2012).
- Shabel, S. J., Proulx, C. D., Trias, A., Murphy, R. T. & Malinow, R. Input to the lateral habenula from the basal ganglia is excitatory, aversive, and suppressed by serotonin. *Neuron* **74**, 475–481 (2012).
- Li, K. *et al.*  $\beta$ CaMKII in lateral habenula mediates core symptoms of depression. *Science* **341**, 1016–1020 (2013).
- Proulx, C. D., Hikosaka, O. & Malinow, R. Reward processing by the lateral habenula in normal and depressive behaviors. *Nat. Neurosci.* **17**, 1146–1152 (2014).
- Shabel, S. J., Proulx, C. D., Piriz, J. & Malinow, R. Mood regulation. GABA/glutamate co-release controls habenula output and is modified by antidepressant treatment. *Science* **345**, 1494–1498 (2014).
- Lecca, S. *et al.* Rescue of GABA<sub>B</sub> and GIRK function in the lateral habenula by protein phosphatase 2A inhibition ameliorates depression-like phenotypes in mice. *Nat. Med.* **22**, 254–261 (2016).
- Yang, Y., Wang, H., Hu, J. & Hu, H. Lateral habenula in the pathophysiology of depression. *Curr. Opin. Neurobiol.* **48**, 90–96 (2017).
- Cui, W. *et al.* Glial dysfunction in the mouse habenula causes depressive-like behaviors and sleep disturbance. *J. Neurosci.* **34**, 16273–16285 (2014).
- Yang, Y. *et al.* Ketamine blocks bursting in the lateral habenula to rapidly relieve depression. *Nature* <http://doi.org/10.1030/nature25509> (2018).
- Henn, F. A. & Vollmayr, B. Stress models of depression: forming genetically vulnerable strains. *Neurosci. Biobehav. Rev.* **29**, 799–804 (2005).
- Adzic, M. *et al.* The contribution of hypothalamic neuroendocrine, neuroplastic and neuroinflammatory processes to lipopolysaccharide-induced depressive-like behaviour in female and male rats: Involvement of glucocorticoid receptor and C/EBP- $\beta$ . *Behav. Brain Res.* **291**, 130–139 (2015).
- Ransom, C. B. & Sontheimer, H. Biophysical and pharmacological characterization of inwardly rectifying K<sup>+</sup> currents in rat spinal cord astrocytes. *J. Neurophysiol.* **73**, 333–346 (1995).
- Djukic, B., Casper, K. B., Philpot, B. D., Chin, L. S. & McCarthy, K. D. Conditional knock-out of Kir4.1 leads to glial membrane depolarization, inhibition of potassium and glutamate uptake, and enhanced short-term synaptic potentiation. *J. Neurosci.* **27**, 11354–11365 (2007).
- Olsen, M. L. & Sontheimer, H. Functional implications for Kir4.1 channels in glial biology: from K<sup>+</sup> buffering to cell differentiation. *J. Neurochem.* **107**, 589–601 (2008).
- Newman, E. & Reichenbach, A. The Müller cell: a functional element of the retina. *Trends Neurosci.* **19**, 307–312 (1996).
- Amédée, T., Robert, A. & Coles, J. A. Potassium homeostasis and glial energy metabolism. *Biol. Cell* **21**, 46–55 (1997).
- Neusch, C. *et al.* Lack of the Kir4.1 channel subunit abolishes K<sup>+</sup> buffering properties of astrocytes in the ventral respiratory group: impact on extracellular K<sup>+</sup> regulation. *J. Neurophysiol.* **95**, 1843–1852 (2006).
- Newman, E. A. Inward-rectifying potassium channels in retinal glial (Müller) cells. *J. Neurosci.* **13**, 3333–3345 (1993).
- Rojas, L. & Orkand, R. K. K<sup>+</sup> channel density increases selectively in the endfoot of retinal glial cells during development of *Rana catesbeiana*. *Glia* **25**, 199–203 (1999).
- Shigetomi, E. *et al.* Imaging calcium microdomains within entire astrocyte territories and endfeet with GCaMPs expressed using adeno-associated viruses. *J. Gen. Physiol.* **141**, 633–647 (2013).
- Hibino, H. *et al.* Inwardly rectifying potassium channels: their structure, function, and physiological roles. *Physiol. Rev.* **90**, 291–366 (2010).

**Supplementary Information** is available in the online version of the paper.

**Acknowledgements** We thank K. McCarthy for Kir4.1 floxed mice; B. Khakh for the GFAP-Kir4.1 plasmid; T. Xue for advice on dn-Kir4.1 design; Y.-Y. Liu for technical support on electromicroscopy; C. Liu and C.-J. Shen for help with immunohistochemistry; S.-M. Duan, Y.-D. Zhou, J.-W. Zhao, X.-H. Zhang and B. MacVicar for advice on experimental design; and C. Giaume and P. Magistretti for comments on the manuscript. This work was supported by grants from the National Key R&D Program of China (2016YFA0501000), the National Natural Science Foundation of China (91432108, 31225010, and 81527901 to H.H., 81701335 to Y.C., and 81730035 to S.W.), the Strategic Priority Research Program (B) of the Chinese Academy of Sciences (XDB02030004) and 111 project (B13026) to H.H.

**Author Contributions** Y.C. performed the *in vitro* patch recordings; Y.Y. performed the biochemistry and immunohistochemistry experiments; Y.C., Y.Y., Y.D. and K.S. performed viral injections and behavioural experiments; Z.N., A.F. and H.B. established the biophysical model; S.M. assisted with cell culture experiments; G.C. and S.W. conducted the electron microscopy experiments; Y.S. contributed Kir4.1 floxed mice; S.T. and Y.L. constructed plasmids; H.H. and Y.C. designed the study; and H.H. wrote the manuscript with the assistance of Y.C., Y.Y. and Z.N.

**Author Information** Reprints and permissions information is available at [www.nature.com/reprints](http://www.nature.com/reprints). The authors declare no competing financial interests. Readers are welcome to comment on the online version of the paper. Publisher's note: Springer Nature remains neutral with regard to jurisdictional claims in published maps and institutional affiliations. Correspondence and requests for materials should be addressed to H.H. ([huhailan@zju.edu.cn](mailto:huhailan@zju.edu.cn)).

**Reviewer Information** *Nature* thanks P. Kenny and the other anonymous reviewer(s) for their contribution to the peer review of this work.

## METHODS

**Animals.** Male cLH rats (3–4 weeks or 8–12 weeks of age) and age-matched male Sprague Dawley rats (SLAC Laboratory Animal Co.) were used. The cLH rats were screened using the learned helplessness test<sup>14,21</sup> for breeding as previously described<sup>21</sup>. Male Wistar rats (SLAC Laboratory Animal Co, 12 weeks) were used for establishing the LPS-induced depressive-like rat model. Male adult (7–8 weeks of age) C57BL/6 mice (SLAC) were used for virus injection in the behaviour experiments. Kir4.1 floxed (*Kcnj10<sup>fl/fl</sup>*) mice (originally obtained from K. McCarthy at University of North Carolina) were used for virus injection in the immunohistochemistry experiments. Animals were group-housed two per cage for rats and four per cage for mice under a 12-h light–dark cycle (light on from 7 a.m. to 7 p.m.) with access to food and water *ad libitum*. All animal studies and experimental procedures were approved by the Animal Care and Use Committee of the animal facility at Zhejiang University.

**Western blotting.** The habenular membrane fraction and whole proteins were extracted as previously described<sup>14</sup>. Animals were anaesthetized using isoflurane, and habenular tissue was quickly dissected from the brain and homogenized in lysis buffer (320 mM sucrose, 4 mM HEPES pH 7.4, 1 mM MgCl<sub>2</sub> and 0.5 mM CaCl<sub>2</sub>, 5 mM NaF, 1 mM Na<sub>3</sub>VO<sub>4</sub>, EDTA-free, protease inhibitor cocktail tablets (Roche) on ice. The lysis buffer used for extracting the total protein of HEK293TN cells contained 50 mM Tris (pH 7.4), 150 mM NaCl, 1% Triton X-100, 1% sodium deoxycholate, 0.1% SDS and protease inhibitor cocktail tablets (Roche). After protein concentration measurement by BCA assay, 10–20 µg protein for each lane was separated on a 10% SDS–PAGE gel and transferred for western blot analysis. Rabbit anti-Kir4.1 intracellular peptide (1:1,000, Alomone labs), mouse anti-GFAP (1:1,000, Sigma), mouse anti-α-tubulin (1:5,000, Sigma) and mouse anti-GAPDH–HRP (1:5,000, KangChen Bio-tech Inc.) antibodies, and high-sensitivity ECL reagent (GE Healthcare) were used. All the bands were analysed with Quantity One or Image J.

**Immunohistochemistry.** Animals were anaesthetized using 10% chloral hydrate, and then perfused transcardially with ice-cold PBS (pH 7.4) followed by 4% paraformaldehyde. After overnight post fix in 4% paraformaldehyde solution, brains were cryoprotected in 30% sucrose for 1 day (for mice) or 3 days (for rats). Coronal sections (40 µm) were cut on a microtome (Leica) and collected in PBS and stored at 4 °C for further use. The antibodies used were rabbit anti-Kir4.1 extracellular peptide (1:200, Alomone labs), mouse anti-GFAP (1:500, Sigma), mouse anti-NeuN (1:500, Millipore), rabbit anti-NeuN (1:500, Millipore), mouse anti-S100β (1:500, Sigma), chicken anti-GFP (1:1,000, Abcam), mouse anti-Flag (1:1,000, Beyotime), Alexa Fluor 488 goat anti-rabbit IgG, Alexa Fluor 488 goat anti-chicken IgG, Alexa Fluor 546 goat anti-mouse IgG (all 1:1,000, Invitrogen). Specifically, for Kir4.1 staining, the rabbit anti-Kir4.1 extracellular peptide antibody was incubated for 48–72 h and the other primary antibodies were incubated for 36–48 h. For the antibody absorption experiments, the rabbit anti-Kir4.1 extracellular peptide antibody was pre-adsorbed with the Kir4.1 extracellular antigen by mixing at a weight ratio of 1:2 for 24 h. Slices for checking the injection site were counterstained with Hoechst in the final incubation step. Fluorescent image acquisition was performed with an Olympus Fluoview FV1000 confocal microscope and a Nikon A1 confocal microscope.

**Cell transfection and cell culture.** Human embryonic kidney (HEK293) cells (gift from J. Luo) were used for the electrophysiology recording and HEK293TN cells (Taitool Bioscience) were used for western blot analysis. Cells used in this study were authenticated and checked for mycoplasma contamination. The plasmids used were pAAV-Ubi-Kir4.1-2A-eGFP, pAAV-Ubi-dnKir4.1 (GYG to AAA)-2A-eGFP, pAAV-CAG-eGFP, pAAV-H1-Kir4.1-shRNA-CAG-eGFP and pAAV-H1-Luciferase-shRNA-CAG-eGFP. HEK293 or HEK293 TN cells were grown in DMEM (HyClone) with 10% FBS (HyClone) at 37 °C and 5% CO<sub>2</sub>. Cells were transfected with appropriate constructs 24 h after plating using Lipofectamine 2000 (Invitrogen) according to the manufacturer's instructions. Culture medium was replaced 5–6 h after transfection. Cells were cultured for another 48 h before western blotting or electrophysiology experiments.

**Plasmid constructs.** The pAAV-Ubi-Kir4.1-2A-eGFP plasmid was assembled by homologous recombination of an AAV backbone linearized from the AAV-Ubi-CaMKIIA-2A-eGFP plasmid<sup>14</sup> by PCR and Kir4.1 amplified from a pZac2.1-gfaABC1D-eGFP-Kir4.1 plasmid (AddGene). The pAAV-Ubi-dnKir4.1 (GYG to AAA)-2A-eGFP plasmid was made by PCR-based mutagenesis using pAAV-Ubi-Kir4.1-2A-eGFP as a backbone (fw: 5'-ACCATTGCGCCGCC TTCCGCTACATCAGCGA-3'; rev: 5'-GGCGGCGGCAATGGTGGTCTGG GATTCGAGGA-3'). The pAAV-gfaABC1D-dnKir4.1 (GYG to AAA)-2A-eGFP plasmid was assembled by homologous recombination of a pZac2.1-gfaABC1D backbone linearized from the pZac2.1-gfaABC1D-eGFP-Kir4.1 plasmid (AddGene) by PCR and a Kir4.1dn-2A-eGFP sequence amplified from the pAAV-Ubi-dnKir4.1 (GYG to AAA)-2A-eGFP plasmid. The pAAV-H1-Kir4.1-shRNA-CAG-eGFP plasmid was constructed using a vector (Taitool Bioscience), which

contains a CAG promoter driving eGFP and an H1 promoter driving shRNA expression. We designed six shRNA sequences using RNAi designer online software (<http://rnaidesigner.thermofisher.com/rnaexpress/>; Invitrogen) as indicated below:

- 1) 5'-GGACGACCTTCATTGACAT-3'
- 2) 5'-GCTACAAGCTTCTGCTCTTCT-3'
- 3) 5'-GCTCTTCTCGCCAACCTTTAC-3'
- 4) 5'-CCGGAACCTTCTGCGAAA-3'
- 5) 5'-GCGTAAGAGTCTCCTCATTGG-3'
- 6) 5'-GCCCTTAGTGTGCGCATTA-3'

We then tested the knockdown efficiency by western blot of Kir4.1 from HEK293TN cells which were co-transfected with Flag-tagged-Kir4.1 plasmid (pAAV-CMV-betaGlobin-Kir4.1-eGFP-3Flag) and each of the six shRNA plasmids. Based on our western blot result (Extended Data Fig. 10a), we chose the fifth sequence, 5'-GCGTAAGAGTCTCCTCATTGG-3', for the Kir4.1-shRNA virus package.

**Electron microscopic immunohistochemistry.** Four mice were deeply anaesthetized with 1% sodium pentobarbital intraperitoneally (50 mg/kg body weight) and perfused transcardially with 20 ml saline, followed by 40 ml ice-cold mixture of 4% paraformaldehyde and 0.05% glutaraldehyde in 0.1 M PB for 1 h. Brains were removed and postfixed by immersion in the same fixative for 4 h at 4 °C. Serial coronal sections of 50 µm thickness were prepared with a vibratome (VT 1000S, Leica), and approximately 18–20 sections, including the LHb region, were collected from each brain.

Kir4.1 was detected by immunogold-silver staining. In brief, sections were blocked with blocking buffer (5% BSA, 5% NGS and 0.05% Triton X-100 in PBS), and then incubated overnight with primary antibodies (rabbit anti-Kir4.1 extracellular peptide; 1:200, Alomone labs) diluted with solution containing 1% BSA, 1% NGS and 0.05% Triton X-100. The secondary antibody was anti-rabbit IgG conjugated to 1.4-nm gold particles (1:100, Nanoprobes) for 4 h. After rinsing, sections were post fixed in 2% glutaraldehyde in PBS for 45 min. Silver enhancement was performed in the dark with HQ Silver Kit (Nanoprobes) for visualization of Kir4.1 immunoreactivity. Before and after the silver enhancement step, sections were rinsed several times with deionized water.

Immunolabelled sections were fixed with 0.5% osmium tetroxide in 0.1 M PB for 1 h, dehydrated in graded ethanol series and then in propylene oxide, and finally flat-embedded in Epon 812 between sheets of plastic. After polymerization, acrylic sheets were then peeled from the polymerized resin, and flat-embedded sections were examined under the light microscope. Three to four sections containing Kir4.1 immunoreactivity in the LHb were selected from each brain, trimmed under a stereomicroscope, and glued onto blank resin stubs. Serial ultrathin sections were cut with an Ultramicrotome (Leica EM UC6, Germany) using a diamond knife (Diatome) and mounted on formvar-coated mesh grids (6–8 sections per grid). They were then counterstained with uranyl acetate and lead citrate, and observed under a JEM-1230 electron microscope (JEOL) equipped with a CCD camera and its application software (832 SC1000).

**Stereotaxic surgery and virus injection.** cLH rats (P50–60) were deeply anaesthetized using 4% pentobarbital. Mice (P50–60 days) were deeply anaesthetized using ketamine (100 mg/kg of body weight) and xylazine (8 mg/kg). Animals were placed on a stereotaxic frame (RWD Instruments). A small volume of virus was injected into the LHb bilaterally (for rats LHb: AP, –3.7 mm from bregma; ML, ±0.7 mm; DV, –4.55 mm from the brain surface; for mice: AP, –1.72 mm from bregma; ML, ±0.46 mm; DV, –2.62 mm from the brain surface) using a pulled glass capillary with a pressure microinjector (Picospritzer III, Parker) at a slow rate of 0.1 µl/min. After the injection was completed, the capillary was left for an additional 10 min before it was then slowly withdrawn completely. After surgery, animals were allowed to recover from anaesthesia under a heat pad.

The following vectors were used: AAV-CaMKIIa::eGFP-Cre (AAV2/1-CaMKIIa-HI-eGFP-Cre, 0.2 µl, bilateral into LHb, University of Pennsylvania vector core), AAV-GFAP::eGFP-Cre (AAV2/5-gfaABC1D-eGFP-Cre, titre: 4.74 × 10<sup>12</sup> v.g./ml, dilution: 1:2, 0.2 µl, bilateral into LHb, Taitool Bioscience), AAV-GFAP::Kir4.1 (AAV2/5-gfaABC1D-eGFP-Kir4.1, titre: 9.19 × 10<sup>12</sup> v.g./ml, dilution: 1:5, 0.2 µl, bilateral into LHb, Taitool Bioscience), AAV-GFAP::eGFP (AAV2/5-gfaABC1D-eGFP, titre: 1.61 × 10<sup>13</sup> v.g./ml, dilution: 1:5, 0.2 µl, bilateral into LHb, University of Massachusetts, Gao Laboratory), AAV-H1::Kir4.1-shRNA (AAV2/5-H1-Kir4.1-shRNA-CAG-eGFP, titre: 3.04 × 10<sup>13</sup> v.g./ml, dilution: 1:10, 0.2 µl, bilateral into LHb, Taitool Bioscience), AAV-H1::Ctrl-shRNA (AAV2/5-H1-Luciferase-shRNA-CAG-eGFP, titre: 1.46 × 10<sup>13</sup> v.g./ml, dilution: 1:5, 0.2 µl, bilateral into LHb, Taitool Bioscience), AAV2/5-gfaABC1D-dnKir4.1-2A-eGFP (GYG to AAA) (titre: 4.15 × 10<sup>13</sup> v.g./ml, 0.2 µl, bilateral into LHb, Taitool Bioscience). All viral vectors were aliquotted and stored at –80 °C until use.

**Depression model and behaviour assay.** LPS-induced depression. The LPS-induced depression model was used as previously described<sup>22</sup>. Wistar male rats

(3 months) were used for the experiments. LPS (Sigma, L-2880) dissolved in sterile 0.9% saline was intraperitoneally injected into Wistar rats, at a dosage of 0.5 mg/kg. This dosage was used to stimulate a subclinical infection without inducing obvious inflammation and other apparent impairments in animals. Saline or LPS was injected between 09:30 and 10:30 a.m. daily for 7 days. The forced swim test was performed 24 h after the last injection. The habenular tissue was dissected 24 h after the behavioural test for western blotting or electrophysiology experiments.

**Learned helplessness test (LHT).** Male juvenile (P30) or adult (P90) cLH rats were tested in a lever-pressing task to evaluate the learned helplessness (LH) phenotype<sup>14</sup>. A cue-light-illuminated lever in the shock chamber was presented, which terminated the shock when rats pressed the lever. Fifteen escapable shocks (0.8 mA) were delivered with a 24-s inter-shock interval. Each shock lasted up to 60 s unless the rat pressed the lever to terminate the shock. Out of the 15 trials, rats that failed to press the lever for more than ten trials were defined as learned helpless (LH), and rats with fewer than five failures were defined as non-learned helpless (NLH).

**Forced swim test (FST).** Animals were individually placed in a cylinder (12 cm diameter, 25 cm height for mice; 20 cm diameter, 50 cm height for rats) of water (23–25 °C) and swam for 6 min under normal light<sup>33</sup>. Water depth was set to prevent animals from touching the bottom with tails or hind limbs. Animal behaviours were videotaped from the side. The immobility time during the last 4 min of the test was counted offline by an observer blinded to the animal treatments. Immobility was defined as time when animals remained floating or motionless with only movements necessary for keeping balance in the water. For rats, an additional pre-test was conducted 24 h before the test, during which rats were individually placed in a cylinder of water under the conditions described above for 15 min.

**Sucrose preference test (SPT).** Animals were single housed and habituated with two bottles of water for 2 days, followed by two bottles of 2% sucrose for 2 days<sup>33</sup>. Animals were then water deprived for 24 h and then exposed to one bottle of 2% sucrose and one bottle of water for 2 h in the dark phase. Bottle positions were switched after 1 h. Total consumption of each fluid was measured and sucrose preference was defined as the average sucrose consumption ratio during the first and second hours. Sucrose consumption ratio was calculated by dividing total consumption of sucrose by total consumption of both water and sucrose.

**Open field test (OFT).** Animals were placed in the centre of an arena (40 cm × 40 cm × 40.5 cm for mice; 100 cm × 100 cm × 40 cm for rats) in a room with dim light for 10 min. A video camera positioned directly above the arena was used to track the movement of each animal (Any-maze, Stoelting).

**LHb brain slice preparation.** Rats (P25–30 or P60–90) and mice (P90) were anaesthetized with isoflurane and 10% chloral hydrate, and then perfused with 20 ml ice-cold ACSF (oxygenated with 95% O<sub>2</sub> + 5% CO<sub>2</sub>) containing (mM): 125 NaCl, 2.5 KCl, 25 NaHCO<sub>3</sub>, 1.25 NaH<sub>2</sub>PO<sub>4</sub>, 1 MgCl<sub>2</sub> and 25 glucose, with 1 mM pyruvate added. The brain was removed as quickly as possible after decapitation and put into chilled and oxygenated ACSF. Coronal slices containing the habenula (350 μm and 300 μm thickness for rats and mice, respectively) were sectioned in cold ACSF with a Leica 2000 vibratome, transferred to ASCF at 32 °C for incubation and recovery for 1 h and then transferred to room temperature. ACSF was continuously gassed with 95% O<sub>2</sub> and 5% CO<sub>2</sub>. Slices were allowed to recover for at least 1 h before recording.

**In vitro electrophysiological recording.** For LHb neuron recordings, currents were measured under whole-cell patch-clamp recordings using pipettes with a typical resistance of 5–6 MΩ filled with internal solution containing (mM) 105 K-gluconate, 30 KCl, 4 Mg-ATP, 0.3 Na-GTP, 0.3 EGTA, 10 HEPES and 10 Na-phosphocreatine, with pH set to 7.35. For the biocytin filling, 5 mg/ml biocytin was added in the internal solution. The external ACSF solution contained (in mM) 125 NaCl, 2.5 KCl, 25 NaHCO<sub>3</sub>, 1.25 NaH<sub>2</sub>PO<sub>4</sub>, 1 MgCl<sub>2</sub> and 25 glucose. Cells were visualized with infrared optics on an upright microscope (BX51WI, Olympus). A MultiClamp 700B amplifier and pCLAMP10 software were used for electrophysiology (Axon Instruments). The series resistance and capacitance were compensated automatically after a stable Gigaseal was formed. Spontaneous neuronal activity was recorded under current-clamp ( $I = 0$  pA) for 60 s consecutively. RMP was determined during the silent period of neuronal spontaneous activity.

To test the effects of TTX (1 μM, Sigma) and BaCl<sub>2</sub> (100 μM, Sigma) on neuronal RMP and spontaneous activity, baselines were recorded for at least for 3 min. Then the drug was perfused into the medium with the arrival of the drug being precisely indicated with a bubble that was added before the transition from normal ACSF to ACSF with drug. The effect of TTX on the RMP and spontaneous activity of LHb neurons stabilized after a few minutes, whereas the effect of BaCl<sub>2</sub> took more than 10 min to stabilize. We thus analysed the effects of TTX and BaCl<sub>2</sub> at 5 and 15 min after perfusion started, respectively.

**Astrocytic whole-cell patch-clamp recordings and Kir4.1 current isolation.** Astrocytes were distinguished from neurons by their small (5–10 μm), oval somata

and distinct electrophysiological features: a hyperpolarized RMP ( $-74 \pm 1$  mV), a low input resistance  $R_{in}$  ( $47 \pm 6$  MΩ), a linear  $I-V$  relationship and an absence of action potentials in response to increased injection currents<sup>34,35</sup>. BaCl<sub>2</sub> (100 μM, Sigma) was applied to isolate Kir4.1 current, which was subtracted from the  $I-V$  curve recorded from  $-120$  mV to 0 mV. Biocytin (Sigma, 5 mg/ml) was dissolved into the patch-clamp pipette solution. After electrophysiological characterization, cells were held for at least 30 min in voltage clamp and constantly injected with a hyperpolarization current (500 ms, 50 pA, 0.5 Hz, 30 min) to allow biocytin filling (performed at 34 °C). Subsequently, slices were fixed overnight in 4% paraformaldehyde at 4 °C. The antibodies used were rabbit anti-NeuN (1:500, Millipore), Alexa Fluor 546 donkey anti-rabbit IgG (1:1,000, Invitrogen) and Cy2-conjugated streptavidin (1:1,000, Jackson ImmunoResearch). Fluorescent image acquisition was performed with a Nikon A1 confocal microscope.

**Tri-compartment model.** A tri-compartment model was constructed including the neuron, the astrocyte and the extracellular space. The model was based on ionic fluxes between these three compartments. Na<sup>+</sup> and K<sup>+</sup> voltage-gated channels, and leak channels were recruited into the neuron as  $dV_N/dt = (I_{app} - I_K - I_{Na} - I_{Leak,N})/C_N$ , where  $V_N$  is the neuronal membrane potential,  $C_N$  is the neuronal capacitance,  $I_{app}$  is an external current applied to the neuron,  $I_{Na}$  and  $I_K$  are the fast Na<sup>+</sup> and K<sup>+</sup> currents of the action potentials, respectively, and  $I_{Leak,N}$  is responsible for the neuronal resting membrane potential. To trigger an action potential, we applied an external step current of amplitude 5 nA and duration 0.1 ms. Kir4.1 channels on the extracellular and vessel side and leak channels were recruited into the astrocyte as  $dV_A/dt = (-I_{Kir} - I_{Kir,vess} - I_{Leak,A})/C_A$ , where  $V_A$  is the astrocytic membrane potential,  $C_A$  is the astrocytic capacitance,  $I_{Kir}$  and  $I_{Kir,vess}$  account for the K<sup>+</sup> flow on the side of the neuron and vessel, respectively ( $I_{Kir}$  is outward during the resting state, and becomes inward when K<sup>+</sup> equilibrium potential exceeds the astrocytic membrane potential), and  $I_{Leak,A}$  is responsible for the astrocytic resting membrane potential.

The dynamics for K<sup>+</sup> in the three compartments are described by:

$$d[K^+]_O/dt = (I_{Kir} + I_K)/(F \times Vol_O) - 2(i_{pump,N} + i_{pump,A}) - d_{K-O}([K^+]_O - K_{O_0})$$

$$d[K^+]_N/dt = -I_K/(F \times Vol_N) + 2i_{pump,N} \times Vol_O/Vol_N - d_{K-N}([K^+]_N - K_{N_0})$$

$$d[K^+]_A/dt = (-I_{Kir} - I_{Kir,vess})/(F \times Vol_A) + 2i_{pump,A} \times Vol_O/Vol_A - d_{K-A}([K^+]_A - K_{A_0})$$

where  $[K^+]_O$ ,  $[K^+]_N$  and  $[K^+]_A$  are the extracellular, neuronal and astrocytic K<sup>+</sup> concentrations, respectively;  $F$  is the Faraday constant;  $Vol_O$ ,  $Vol_A$  and  $Vol_N$  are the volumes of the extracellular, astrocytic and neuronal compartments, respectively; and  $i_{pump,N}$  and  $i_{pump,A}$  are the fluxes through the Na<sup>+</sup>/K<sup>+</sup> pump of the neuron and astrocyte membranes, respectively. The term  $d([X] - [X_0])$  describes the diffusion of K<sup>+</sup> in the considered compartment, where  $d_{K-O}$ ,  $d_{K-N}$  and  $d_{K-A}$  are the rates of extracellular, neuronal and astrocytic K<sup>+</sup> effective flux;  $K_{O_0}$ ,  $K_{N_0}$  and  $K_{A_0}$  are the extracellular, neuronal and astrocytic K<sup>+</sup> concentrations expected at equilibrium, respectively. The extracellular K<sup>+</sup> is mainly contributed by  $I_K$ . Released extracellular K<sup>+</sup> from the neuron is taken up by Kir4.1 channels and Na<sup>+</sup>/K<sup>+</sup> pumps.

The dynamics for Na<sup>+</sup> in the three compartments are described by:

$$d[Na^+]_O/dt = I_{Na}/(F \times Vol_O) + 3(i_{pump,N} + i_{pump,A}) - d_{Na-O}([Na^+]_O - Na_{O_0})$$

$$d[Na^+]_N/dt = -I_{Na}/(F \times Vol_N) - 3i_{pump,N} \times Vol_O/Vol_N - d_{Na-N}([Na^+]_N - Na_{N_0})$$

$$d[Na^+]_A/dt = -3i_{pump,A} \times Vol_O/Vol_A - d_{Na-A}([Na^+]_A - Na_{A_0})$$

See Supplementary Information (Model Description and Supplementary Table 2) for detailed formulae.

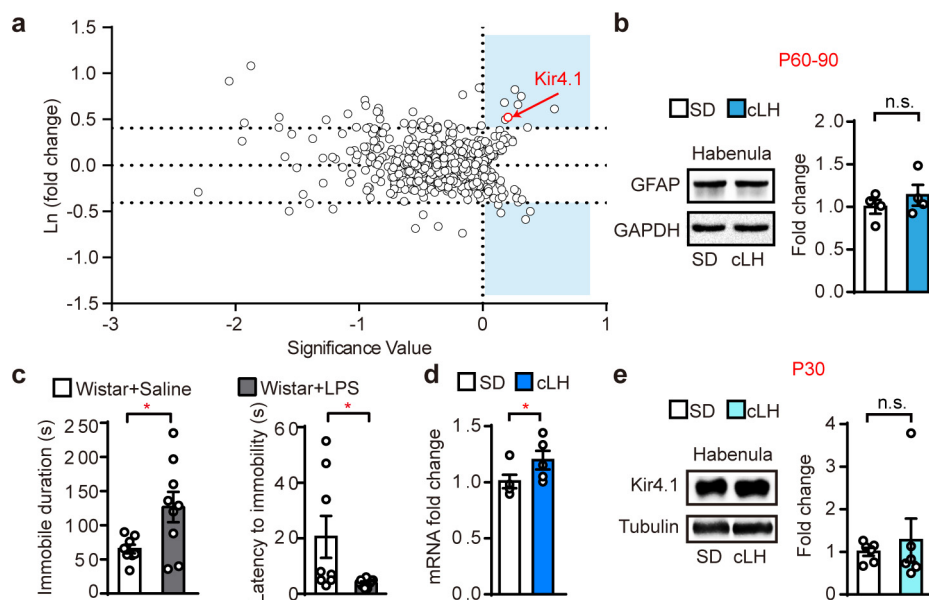
**Statistical analyses.** The required sample sizes were estimated on the basis of our past experience performing similar experiments. Animals were randomly assigned to treatment groups. Analyses were performed blinded to treatment assignments in all behavioural experiments. Statistical analyses were performed using GraphPad Prism software v6. By pre-established criteria, values were excluded from the

analyses if the viral injection or drug delivering sites were out of the LHb. All statistical tests were two-tailed, and significance was assigned at  $P < 0.05$ . Normality and equal variances between group samples were assessed using the D'Agostino and Pearson omnibus normality test and Brown–Forsythe tests, respectively. When normality and equal variance between sample groups was achieved, one-way ANOVAs (followed by Bonferroni's multiple comparisons test) or  $t$ -tests were used. Where normality or equal variance of samples failed, Mann–Whitney  $U$  tests were performed. Linear regression tests and  $\chi^2$  tests were used in appropriate situations. The sample sizes, specific statistical tests used,

and main effects of our statistical analyses for each experiment are reported in Supplementary Table 1.

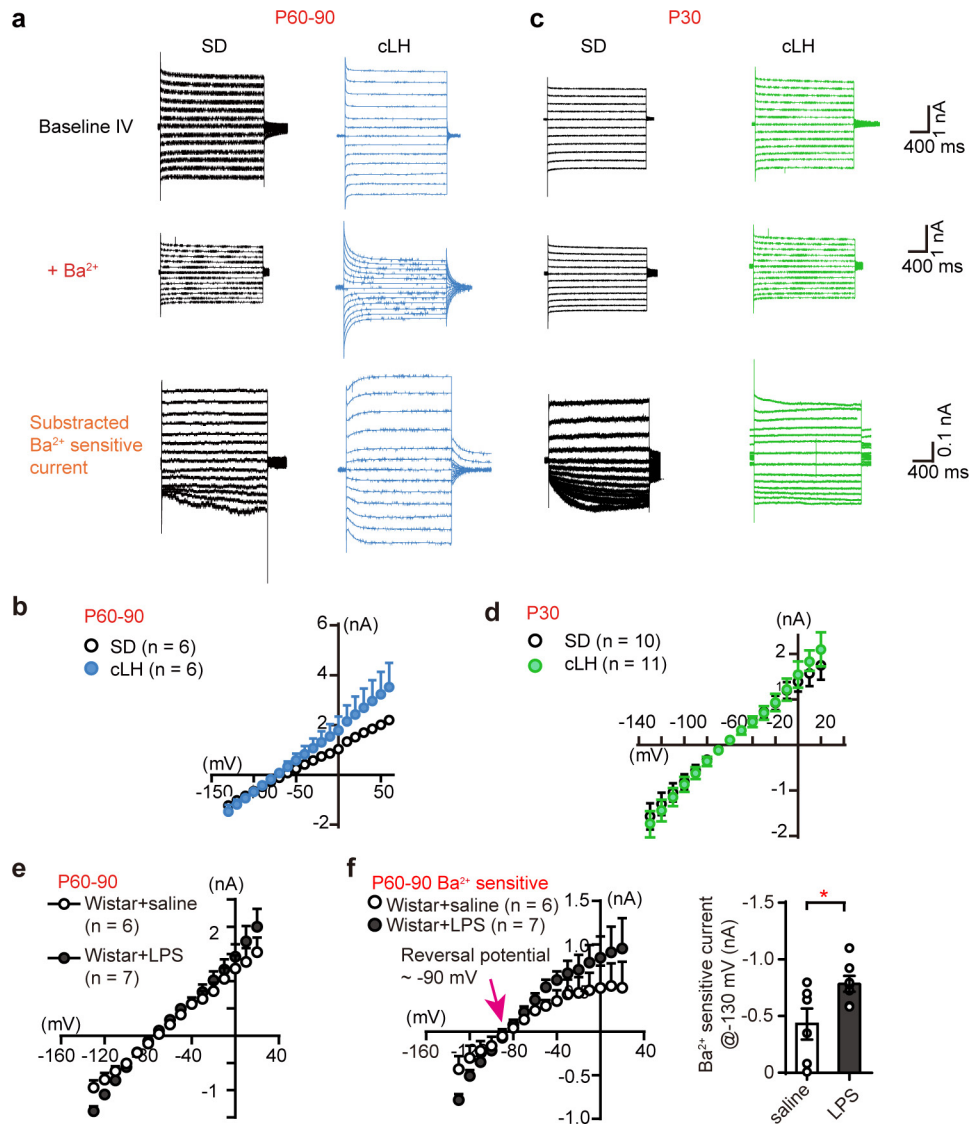
**Data availability.** The data that support the findings of this study are available from the corresponding author upon reasonable request.

33. Powell, T. R., Fernandes, C & Schalkwyk, L. C. *Depression-Related Behavioral Tests* (John Wiley & Sons, 2011).
34. Verkhratskii, A. N & Butt, A. *Glial Neurobiology: a Textbook* (John Wiley & Sons, 2007).
35. Kettenmann, H & Ransom, B. R. *Neuroglia* 3rd edn (Oxford Univ. Press, 2013).



**Extended Data Figure 1 | Habenular protein expression in rat models of depression.** **a**, Volcano plot of high-throughput proteomic screen identifies proteins that are differentially expressed in the habenulae of cLH rats versus wild-type rats. Ln (fold change) is ln-transformed value of the normalized protein ratio of cLH and control<sup>14</sup>. Significance value was calculated as the average normalized ratio minus two folds of s.d.<sup>14</sup>. Proteins in the shaded areas have more than 50% significant change. Kir4.1 is one of the eight upregulated proteins identified<sup>14</sup>. Dashed lines indicate fold change of 50%. **b**, Western blot analysis showing no change in

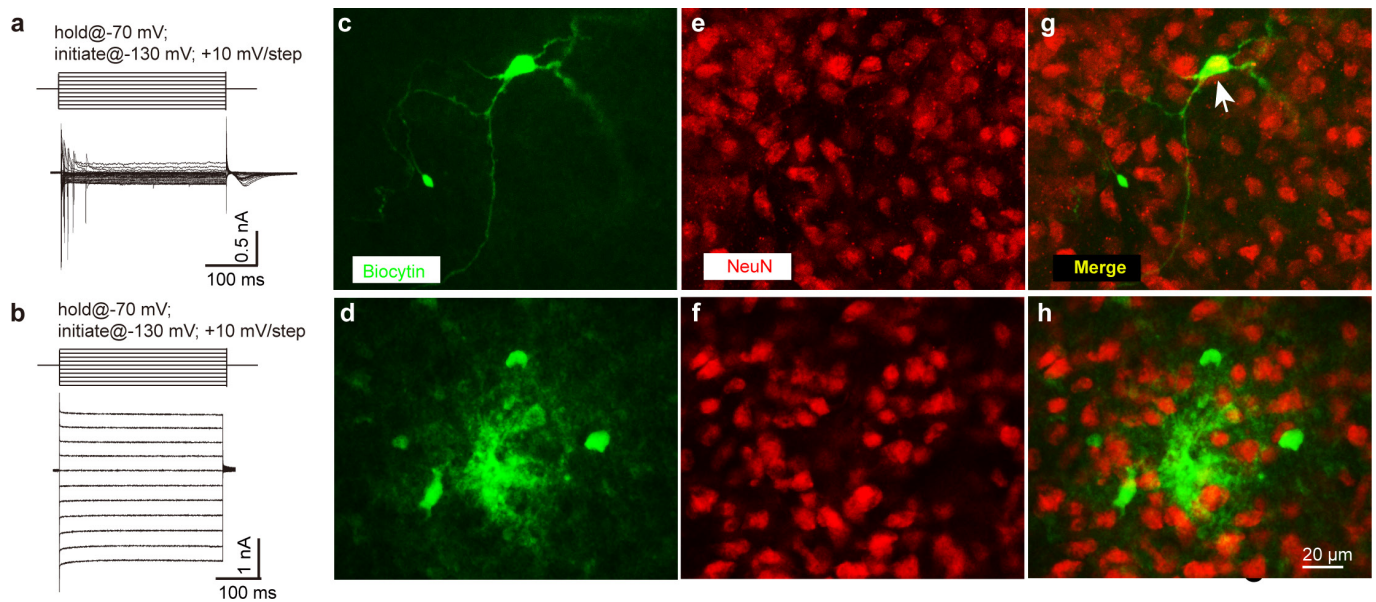
GFAP protein in habenulae of cLH rats at P60–90.  $n = 4$ , 4 rats for control and cLH, respectively. **c**, LPS injection ( $500 \mu\text{g kg}^{-1}$  i.p. for 7 days) induces increased immobile time and decreased latency to immobility in the FST.  $n = 8$ , 9 rats for saline and LPS, respectively. **d**, QPCR analysis of Kir4.1 mRNA in habenulae. Two-tailed paired  $t$ -test.  $n = 5$ , 5 rats for control and cLH, respectively. **e**, Western blot analysis showing no change in Kir4.1 protein in membrane fraction of habenulae in cLH rats at P30.  $n = 6$ , 6. Data are means  $\pm$  s.e.m., \* $P < 0.05$ , n.s., not significant. Two-tailed paired  $t$ -test (**b**, **d**, **e**); two-tailed unpaired  $t$ -test (**c**).



**Extended Data Figure 2 | Ba<sup>2+</sup>-sensitive Kir4.1 current is upregulated in LHb of adult cLH rats and adult LPS-injected Wistar rats.**

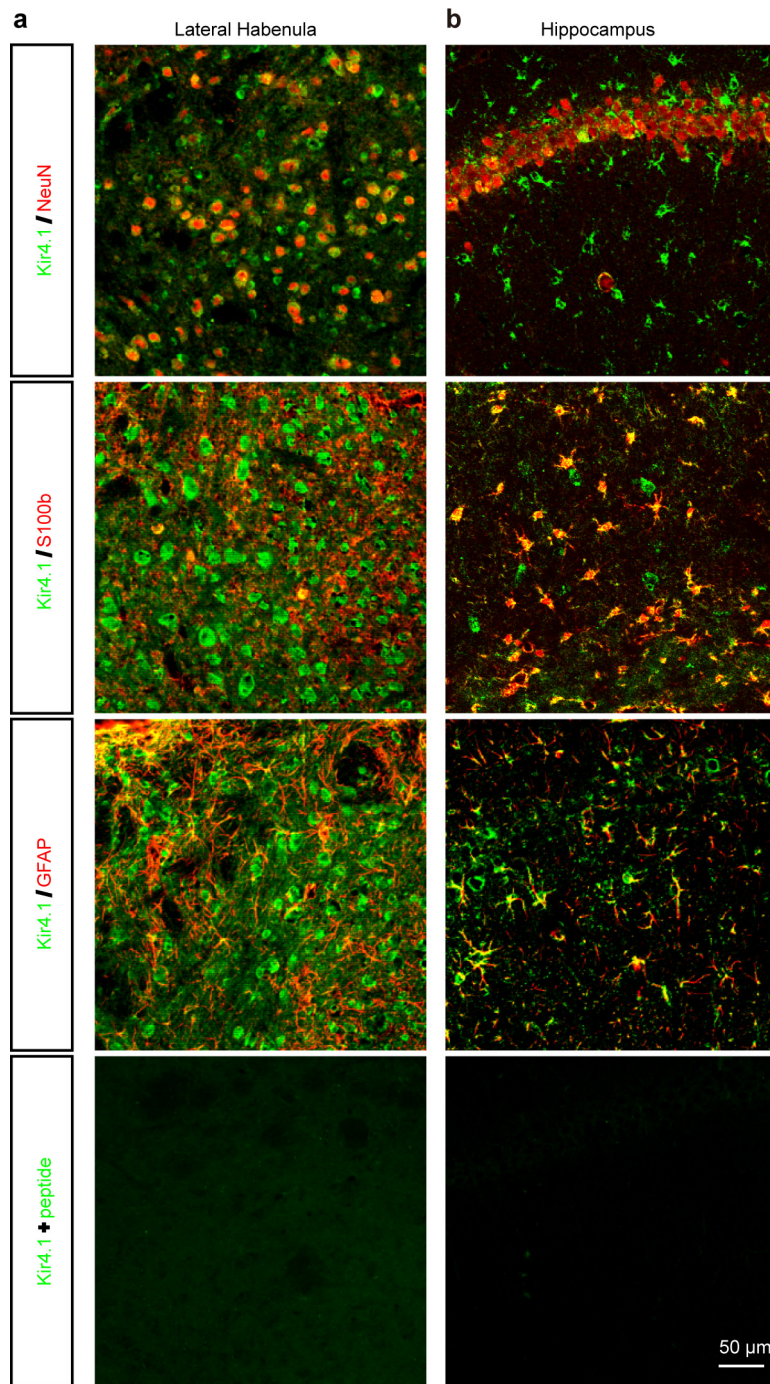
**a, c,** Representative traces showing linear *I-V* curve in a typical astrocyte before (upper) and after (middle) Ba<sup>2+</sup> perfusion under voltage steps (-130 mV to -30 mV, step by 10 mV, 2 s duration, holding at -70 mV). Subtraction of the two led to Ba<sup>2+</sup>-sensitive Kir current (bottom) at P60-90 (**a**) and P30 (**c**) in cLH rats. **b, d,** *I-V* plots of astrocytes in cLH rats

and controls at P60-90 (**b**) and P30 (**d**). **e,** *I-V* plots of astrocytes in LPS-injected Wistar rats and saline controls at P60-90. **f,** *I-V* plot and bar graph showing Ba<sup>2+</sup>-sensitive currents in LPS-injected Wistar rats and saline-injected controls at P60-90. Two-tailed unpaired *t*-test. *n* = 7, 6 astrocytes from 2, 2 rats for saline and LPS, respectively. Data are means ± s.e.m., \**P* < 0.05.



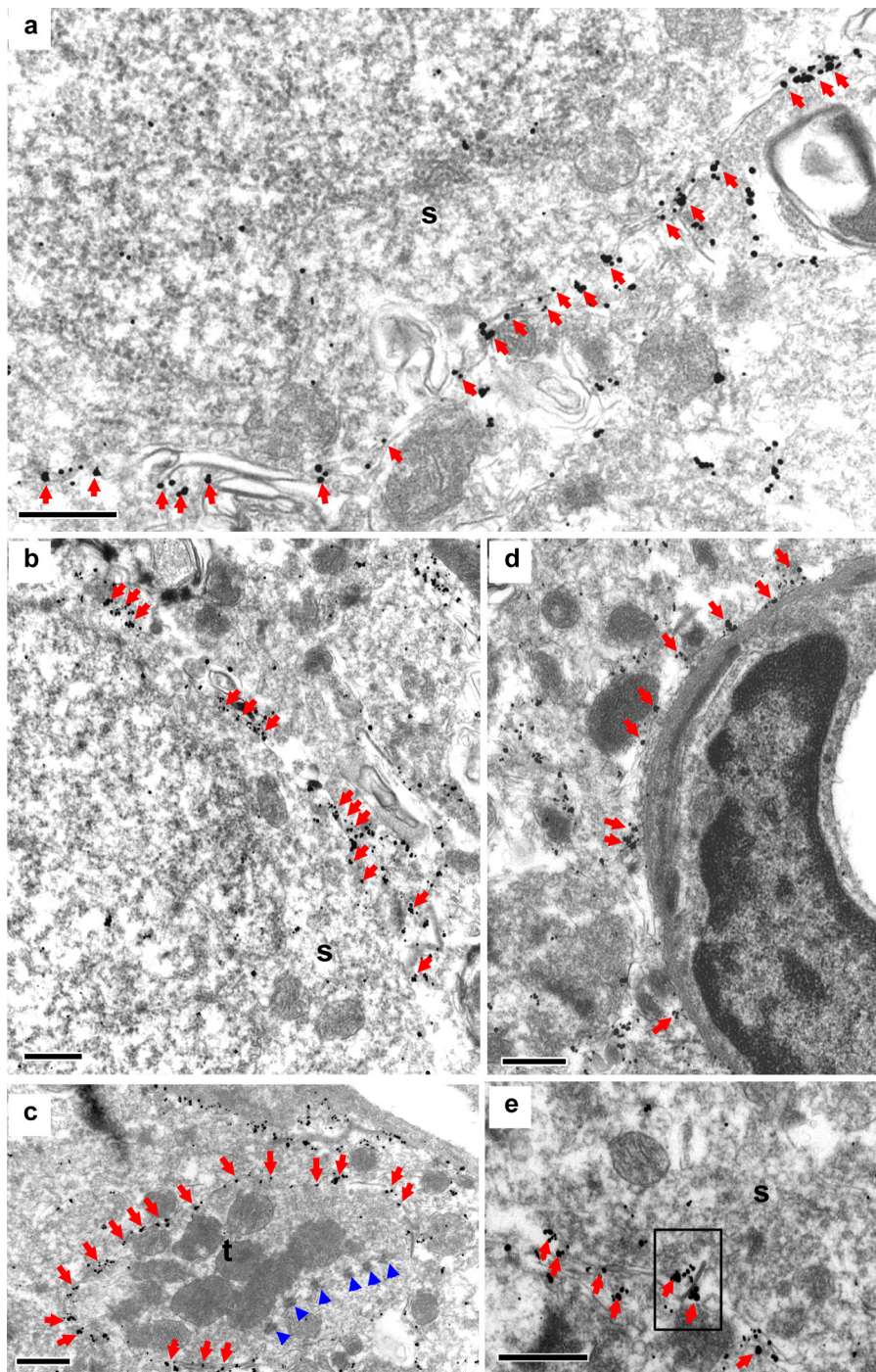
**Extended Data Figure 3 | Biocytin intercellular filling and double staining with NeuN confirm the identity of electrophysiologically identified neurons and astrocytes.** **a, b**, A neuron (**a**) and an astrocyte (**b**) in LHb slices were first identified on the basis of their specific morphology (astrocytes: 5–10  $\mu$ m diameter; neurons:  $\sim$ 15  $\mu$ m diameter) and physiological properties. The neuron fires at a depolarizing voltage step (**a**), whereas the astrocyte shows a steady-state  $I$ – $V$  relationship and a lack of spiking activity (**b**). After electrophysiological characterization, cells were held for at least 30 min in voltage clamp and constantly injected with a hyperpolarization current (500 ms, 50 pA, 0.5 Hz, 30 min) to allow biocytin

filling. **c–h**, Biocytin-labelled neurons and astrocytes subsequently confirmed by co-labelling with NeuN. **c, d**, Biocytin signals in a single neuron (**c**) or a group of astrocytes owing to diffusion through gap junctions (**d**) (four independent experiments). **e, f**, NeuN signals (four independent experiments). **g, h**, Colabelling of NeuN with the neuron (indicated by white arrow, **g**) but not astrocytes (**h**) (four independent experiments). Note that all biocytin-filled neurons ( $n = 18$ ) colabel with NeuN and all biocytin-filled astrocytes ( $n = 11$ ) do not colabel with NeuN.



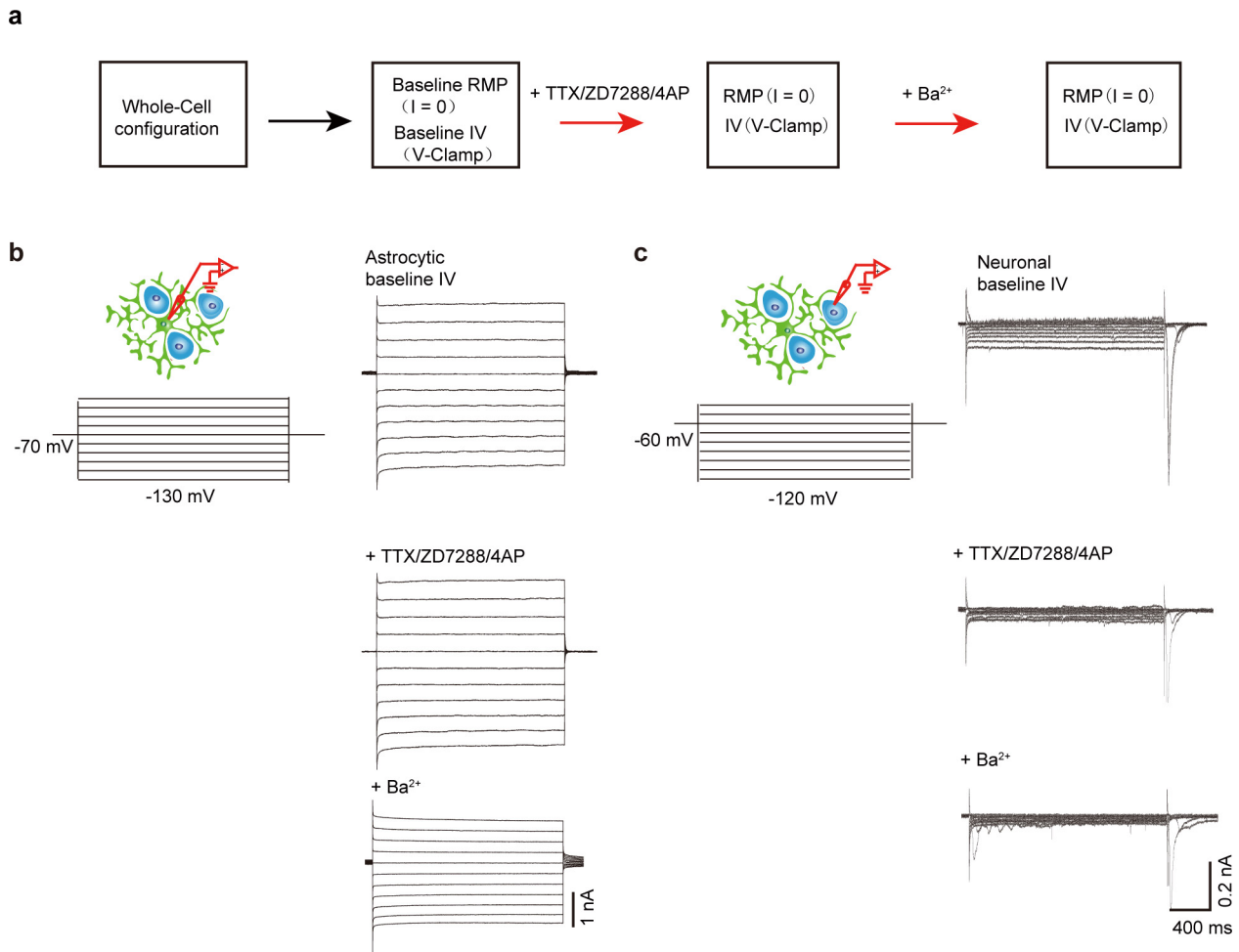
**Extended Data Figure 4 | Expression pattern of Kir4.1 in the LHb and hippocampus. a, b,** Kir4.1 co-immunostaining with neuronal marker (NeuN) or astrocytic marker (S100b and GFAP) in the LHb (a) or

hippocampus (b). Bottom two panels show staining with the same Kir4.1 antibody pre-incubated with the antigen peptide, demonstrating the specificity of the Kir4.1 antibody (two independent experiments).



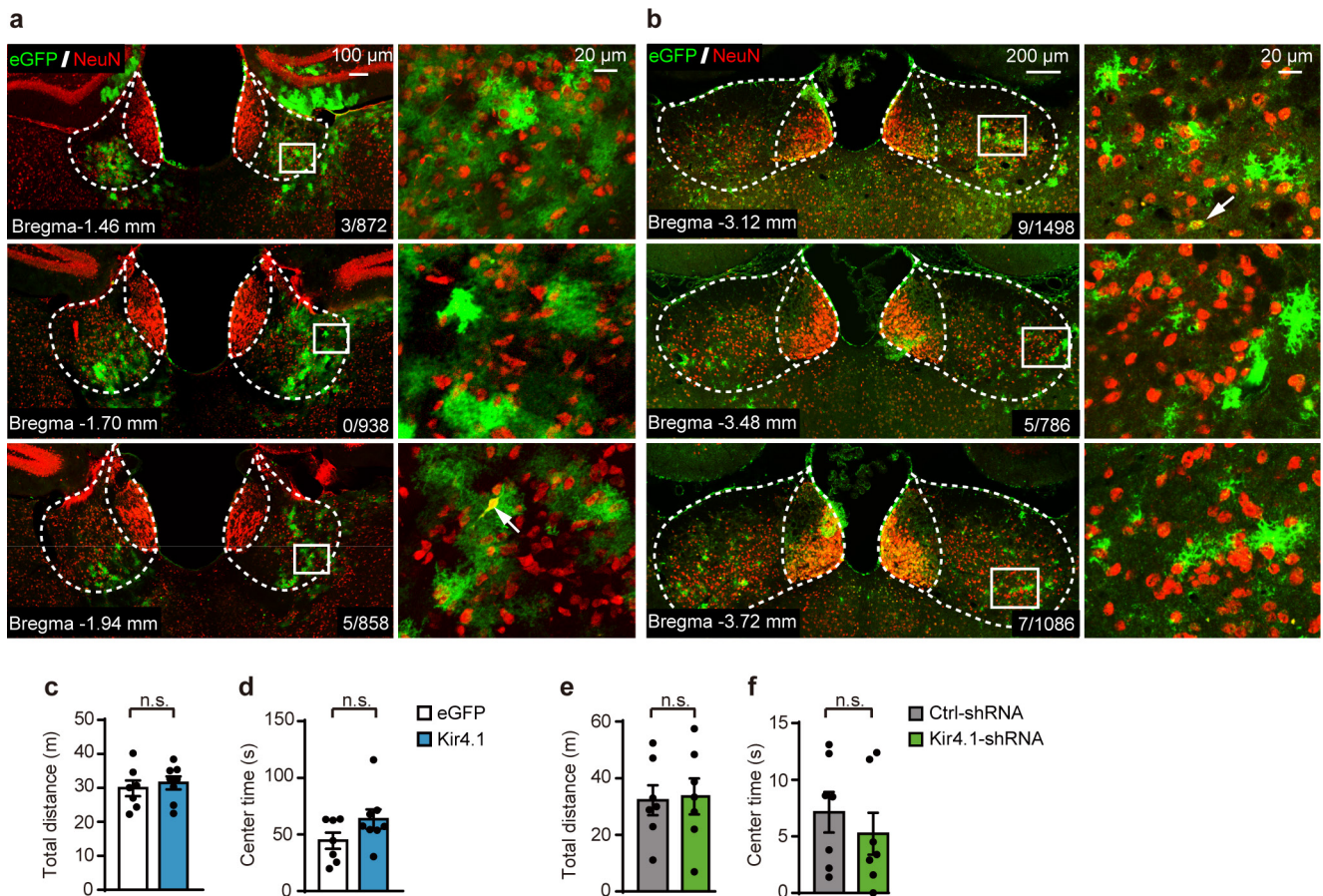
**Extended Data Figure 5 | Electron microscopy immunohistochemistry of Kir4.1 staining.** **a, b,** Many Kir4.1 immunograin (arrows) surround the neuronal soma. **c,** Kir4.1 grains (arrows) also surround axon–dendrite synapses, but are rare near the synaptic zones as indicated by

the postsynaptic densities (arrowheads). **d,** Kir4.1 immunograin are also detected surrounding a vascular endothelial cell. **e,** Inset shows Kir4.1 immunograin near a gap junction. s, neuronal soma; t, axon terminal. Scale bars, 0.5  $\mu\text{m}$ . Three independent experiments.



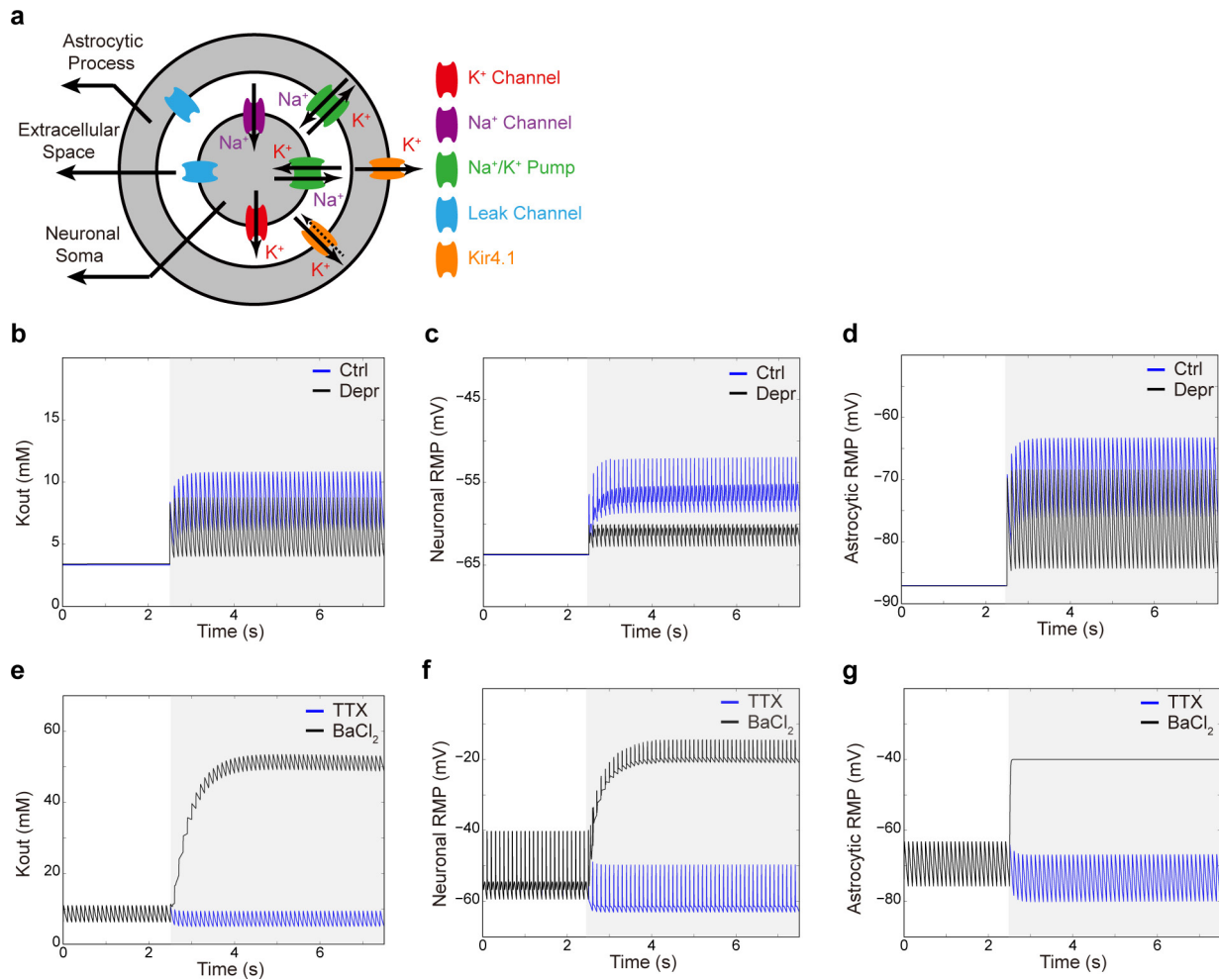
**Extended Data Figure 6 | Kir4.1 is expressed in astrocytes but not neurons in the LHB.** **a**, Schematics showing sequence of drug application and recording after a neuron or astrocyte is patched. **b**, Representative traces showing a linear  $I-V$  curve in a typical astrocyte under voltage steps ( $-130$  mV to  $-30$  mV, step by  $10$  mV,  $2$  s duration, holding at  $-70$  mV, protocol demonstrated on left, upper panel).  $I-V$  curves of the same cell after addition of TTX ( $1$   $\mu$ M), 4-aminopyridine ( $4$ AP,  $1$  mM) and

4-(*N*-ethyl-*N*-phenylamino)-1,2-dimethyl-6-(methylamino) pyrimidinium chloride (ZD7288,  $50$   $\mu$ M) (middle) and further addition of  $Ba^{2+}$  ( $100$   $\mu$ M, bottom) are shown below. **c**, Representative traces showing a nonlinear  $I-V$  curve in a typical neuron under voltage steps ( $-120$  mV to  $-40$  mV, step by  $10$  mV,  $2$  s duration, holding at  $-60$  mV, protocol demonstrated on left, upper panel).  $I-V$  curves of the same cell after addition of TTX, ZD7288 and 4AP (middle) and further addition of  $Ba^{2+}$  (bottom) are shown below.



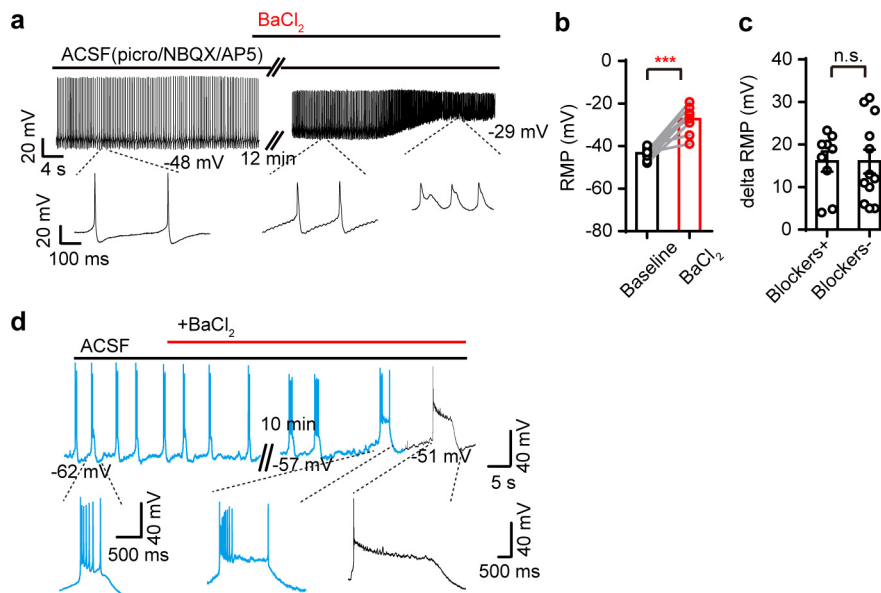
**Extended Data Figure 7 | Characterization of cell-type specificity of *GFAP* promoter, and locomotion.** **a, b**, Double immunofluorescence for NeuN (red) and eGFP (green) in the coronal section of Lhb brain slices infected with AAV-GFAP::Kir4.1 (AAV2/5-gfaABC1D-eGFP-Kir4.1) virus in mice (three independent experiments, **a**) or AAV-GFAP::dnKir4.1 (AAV2/5-gfaABC1D-dnKir4.1-2A-eGFP) virus in cLH rats (two independent experiments, **b**). Left, examples of anterior, middle and posterior coronal sections of Lhb. Numbers in the bottom right corner are the number of merged cells/number of NeuN<sup>+</sup> cells in the virus-infected

area. Right, zoomed-in images of the white square area in left. Note that there is only one infected neuron, as indicated by the white arrow, in all three fields of view. **c, d**, Overexpression of Kir4.1 in the Lhb of C57 mice does not affect locomotion.  $n = 7, 8$  mice for eGFP and Kir4.1, respectively. **e, f**, Overexpression of Kir4.1-shRNA in the Lhb of cLH rats does not affect locomotion activities.  $n = 7, 7$  rats for control and Kir4.1 shRNA, respectively. Data are means  $\pm$  s.e.m; n.s., not significant. Two-tailed unpaired *t*-test (**c-f**).



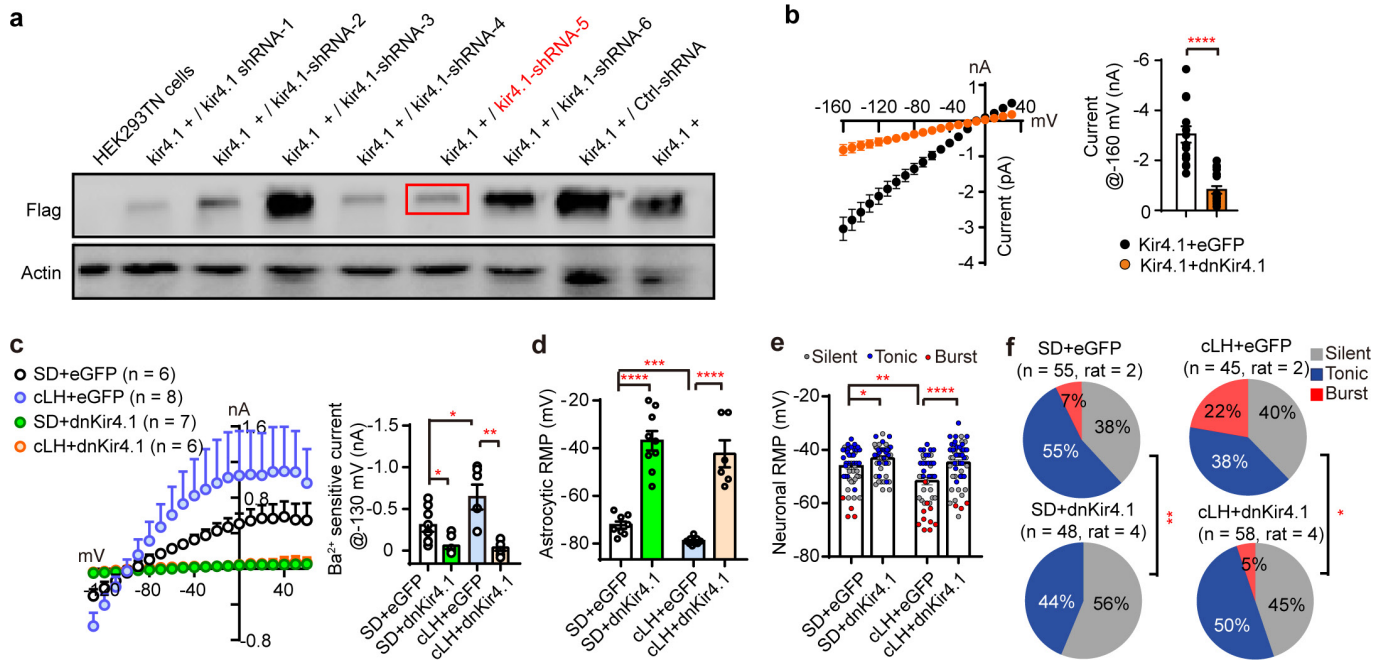
**Extended Data Figure 8 | Simulation of the dynamic potassium buffering effect of Kir4.1 in the tri-compartment model.** **a**, Schematic representation of a tri-compartment model involving neuron, astrocyte and extracellular space (see Methods for details). **b–d**, Effects of increasing Kir4.1 expression on  $[K]_{out}$  (**b**), neuronal membrane potential (**c**) and astrocytic membrane potential (**d**). Ctrl, control condition with  $1 \times Kir4.1$  conductance; Depr, depression condition with  $2 \times Kir4.1$  conductance. Grey shaded areas indicate application of 10 Hz tonic stimulation to neurons. Note that under this neuronal firing condition,  $[K]_{out}$  is lower,

and neuron and astrocyte are more hyperpolarized in the depression condition than the control. **e–g**, Effects of *in silico* TTX (blocking action potentials,  $g_{Na} = 0$ ) or  $Ba^{2+}$  (blocking Kir4.1,  $g_{Kir4.1} = 0$ ) treatments on  $[K]_{out}$  (**e**), neuronal membrane potential (**f**) and astrocytic membrane potential (**g**) when neurons are under 10 Hz tonic stimulation. Grey shaded areas indicate *in silico* application of drugs. Note that TTX and  $Ba^{2+}$  cause opposite changes to  $[K]_{out}$ , neuronal membrane potential and astrocytic membrane potential. Neuronal spikes are not shown for clarity of presentation.



**Extended Data Figure 9 | BaCl<sub>2</sub> caused depolarization of neuronal RMP in the presence of synaptic transmitter blockers.** **a, b**, Representative trace (**a**) and bar graph ( $n = 9$  neurons from 3 rats; **b**) showing effect of BaCl<sub>2</sub> (100  $\mu$ M) perfusion onto tonic-firing neurons that have been bathed with transmitter blockers (100  $\mu$ M picrotoxin, 10  $\mu$ M NBQX and 100  $\mu$ M AP5). **c**, Bar graph showing the level of RMP depolarization caused by BaCl<sub>2</sub> in the presence or absence of transmitter blockers.

$n = 9$ , 12 neurons from 3, 3 rats for with and without blockers, respectively. **d**, Representative trace showing effect of BaCl<sub>2</sub> (sampled 15 min after drug perfusion) on bursting neurons ( $n = 4$  out of 9 neurons from 3 rats). Spikes in bursting and tonic-firing mode are shown in blue and black, respectively. Data are means  $\pm$  s.e.m., \*\*\* $P < 0.001$ , n.s., not significant. Two-tailed paired  $t$ -test (**b**) and two-tailed unpaired  $t$ -test (**c**).



**Extended Data Figure 10 | Characterization of Kir4.1 loss-of-function constructs.** **a**, Flag-tagged-Kir4.1 plasmid (pAAV-CMV-betaGlobin-Kir4.1-eGFP-3Flag) was co-transfected with pAAV-vector expressing six different shRNAs (see Methods) of Kir4.1 or the negative control (shRNA of luciferase) into HEK293 TN cells. On the basis of knockdown efficiency as shown in the western blot, Kir4.1-shRNA-5 was chosen for viral package (two independent experiments). **b**, *I-V* plot showing Kir4.1 currents recorded in HEK293 cells transfected with pAAV-Kir4.1 together with negative control pAAV-eGFP or pAAV-dnKir4.1 plasmid. Bars represent the current values recorded at -160 mV. *n* = 18, 15 HEK293 cells

for eGFP and dnKir4.1, respectively. **c**, *I-V* plot and bar graph showing Ba<sup>2+</sup>-sensitive currents blocked by AAV-dnKir4.1 in both cLH and wild-type rats. **d-f**, AAV-dnKir4.1 caused depolarization of RMP in astrocytes (*n* = 9, 8, 9, 6 astrocytes from 2, 4, 2, 4 rats for wild-type eGFP, wild-type dnKir4.1, cLH eGFP and cLH dnKir4.1, respectively; **d**) and neurons in viral infected area (*n* = 54, 48, 45, 58 neurons from 2, 4, 2, 4 rats, **e**), and abolished neuronal bursting (**f**) in both cLH and wild-type rats. Data are means ± s.e.m.; \**P* < 0.05, \*\**P* < 0.01, \*\*\**P* < 0.001, \*\*\*\**P* < 0.0001. Two-tailed unpaired *t*-test (**b-e**) and  $\chi^2$  test (**f**).

## Life Sciences Reporting Summary

Nature Research wishes to improve the reproducibility of the work that we publish. This form is intended for publication with all accepted life science papers and provides structure for consistency and transparency in reporting. Every life science submission will use this form; some list items might not apply to an individual manuscript, but all fields must be completed for clarity.

For further information on the points included in this form, see [Reporting Life Sciences Research](#). For further information on Nature Research policies, including our [data availability policy](#), see [Authors & Referees](#) and the [Editorial Policy Checklist](#).

### ► Experimental design

#### 1. Sample size

Describe how sample size was determined.

Required sample sizes were estimated based on our past experience performing similar experiments.

#### 2. Data exclusions

Describe any data exclusions.

Values were excluded from the analyses if the viral injection sites were out of LHB.

#### 3. Replication

Describe whether the experimental findings were reliably reproduced.

The experiment for each experiment was successfully repeated for at least two times.

#### 4. Randomization

Describe how samples/organisms/participants were allocated into experimental groups.

Animals were randomly assigned to treatment groups.

#### 5. Blinding

Describe whether the investigators were blinded to group allocation during data collection and/or analysis.

Analysis were performed in a manner blinded to treatment assignments in all behavioral experiments.

Note: all studies involving animals and/or human research participants must disclose whether blinding and randomization were used.

#### 6. Statistical parameters

For all figures and tables that use statistical methods, confirm that the following items are present in relevant figure legends (or in the Methods section if additional space is needed).

n/a | Confirmed

- The exact sample size ( $n$ ) for each experimental group/condition, given as a discrete number and unit of measurement (animals, litters, cultures, etc.)
- A description of how samples were collected, noting whether measurements were taken from distinct samples or whether the same sample was measured repeatedly
- A statement indicating how many times each experiment was replicated
- The statistical test(s) used and whether they are one- or two-sided (note: only common tests should be described solely by name; more complex techniques should be described in the Methods section)
- A description of any assumptions or corrections, such as an adjustment for multiple comparisons
- The test results (e.g.  $P$  values) given as exact values whenever possible and with confidence intervals noted
- A clear description of statistics including central tendency (e.g. median, mean) and variation (e.g. standard deviation, interquartile range)
- Clearly defined error bars

See the web collection on [statistics for biologists](#) for further resources and guidance.

## ► Software

Policy information about [availability of computer code](#)

### 7. Software

Describe the software used to analyze the data in this study.

MATLAB was used for the simulation. GraphPad Prism software v6 were used for statistical analyses.

For manuscripts utilizing custom algorithms or software that are central to the paper but not yet described in the published literature, software must be made available to editors and reviewers upon request. We strongly encourage code deposition in a community repository (e.g. GitHub). *Nature Methods* [guidance for providing algorithms and software for publication](#) provides further information on this topic.

## ► Materials and reagents

Policy information about [availability of materials](#)

### 8. Materials availability

Indicate whether there are restrictions on availability of unique materials or if these materials are only available for distribution by a for-profit company.

cLH rats need permission from Fritz Henn. Other unique materials used are readily available from the authors or commercially available.

### 9. Antibodies

Describe the antibodies used and how they were validated for use in the system under study (i.e. assay and species).

Rabbit anti-Kir4.1 (intracellular) (Alomone labs, APC-035), rabbit anti-Kir4.1 (extracellular) (Alomone labs, APC-165), mouse anti- $\alpha$  tubulin (Sigma, T6074), mouse anti-GAPDH-HRP (KangChen Bio-tech Inc, KC-5G5), mouse anti-GFAP (Sigma, G3893), mouse anti-NeuN (Millipore, MAB377), rabbit anti-NeuN (Millipore, MABN140), mouse anti-S100B (Sigma, AMAB91038), chicken anti-GFP (Abcam, ab13970), mouse anti-Flag (Beyotime, AF519).

### 10. Eukaryotic cell lines

a. State the source of each eukaryotic cell line used.

HEK293 cells (gift from Jianhong Luo) were used for the electrophysiology recording and HEK293TN cells (Taitool Bioscience, China) were used for western blot analysis.

b. Describe the method of cell line authentication used.

Identity of the cell lines were frequently checked by their morphological features.

c. Report whether the cell lines were tested for mycoplasma contamination.

Cells used in this study were checked for mycoplasma contamination.

d. If any of the cell lines used are listed in the database of commonly misidentified cell lines maintained by [ICLAC](#), provide a scientific rationale for their use.

No commonly misidentified cell lines are used in this study.

## ► Animals and human research participants

Policy information about [studies involving animals](#); when reporting animal research, follow the [ARRIVE guidelines](#)

### 11. Description of research animals

Provide details on animals and/or animal-derived materials used in the study.

Male cLH rats (3-4 weeks or 8-12 weeks of age) and age-matched male Sprague Dawley rats (SLAC Laboratory Animal Co., Shanghai) were used. The cLH rats were screened by learned helpless test, for breeding as previously described. Male Wistar rats (SLAC Laboratory Animal Co., Shanghai, 12 weeks) were used for establishing the LPS-induced depressive-like rat model. Male adult (7-8 weeks of age) C57BL/6 mice (SLAC) or Kir4.1f/f floxed mice (originally obtained from Dr. Ken McCarthy at University of North Carolina) were used for virus injection the immunohistochemistry experiments.

Policy information about [studies involving human research participants](#)

### 12. Description of human research participants

Describe the covariate-relevant population characteristics of the human research participants.

No human research participants.